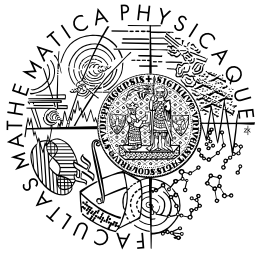

FACULTY
OF MATHEMATICS
AND PHYSICS
Charles University

DOCTORAL THESIS

Alžběta Kadlecová

Quantum Electronic Transport in Superconducting Quantum Dots

Department of Condensed Matter Physics

Supervisor of the doctoral thesis: doc. RNDr. Tomáš Novotný, Ph.D.

Study programme: Physics of Condensed Matter and Materials Research

Prague 2021

I declare that I carried out this doctoral thesis independently, and only with the cited sources, literature and other professional sources. It has not been used to obtain another or the same degree.

I understand that my work relates to the rights and obligations under the Act No. 121/2000 Sb., the Copyright Act, as amended, in particular the fact that the Charles University has the right to conclude a license agreement on the use of this work as a school work pursuant to Section 60 subsection 1 of the Copyright Act.

In ..... date ....

Author's signature

I wish to express my deep gratitude to my supervisor doc. RNDr. Tomáš Novotný, Ph.D., for his guidance in navigating the complex field of superconducting nanostructures, for his patience with my progress, and for all the support I have received during my doctoral studies, both scientific and personal.

I also thank my advisor RNDr. Martin Žonda, Ph.D., for introducing me to the intricacies of the numerical renormalization group method, and all my collaborators for co-creating the research endeavours that I've been part of.

A very special thank you goes to my parents who have raised me with a deep love for logic and science; to my partner, who has been there for me throughout my years of studying; and to the Šamanka tearoom in Prague, which has been my refuge in hard times.

Title: Quantum Electronic Transport in Superconducting Quantum Dots

Author: Alžběta Kadlecová

Department: Department of Condensed Matter Physics

Supervisor: doc. RNDr. Tomáš Novotný, Ph.D., Department of Condensed Matter Physics

Abstract:

In this thesis, the single-level correlated quantum dot attached to two BCS superconducting leads is analyzed. A difference in the superconducting phases of the leads induces the DC Josephson supercurrent in the junction. In this setup, the influence of asymmetrical dot-lead couplings on transport properties is clarified analytically. The coupling asymmetry and the phase difference can be combined into one function, which allows us to calculate physical properties of a system with coupling asymmetry from the properties of its effective symmetric counterpart. The coupling asymmetry turns out to be an important parameter which influences the position of the $0-\pi$ quantum phase transition even in the strongly correlated Kondo regime.

Further, this thesis contributes to the interpretation of an AC Josephson current measurement, in which a surprising drop in the amplitude was observed in the Kondo regime. The experimental setup is characterized using numerical renormalization group calculations of the equilibrium many-body spectra. Possible quantum-point-contact-based interpretations are discussed. Although a drop in the AC Josephson current at the experimental bias voltage is also expected in a quantum point contact, we conclude that the physical mechanisms causing it in the quantum dot system are likely not the same.

Keywords: Quantum dot, Superconductivity, Josephson effect, Nanostructures.

Contents

Introduction

This thesis deals with a mesoscopic "superconducting quantum dot", a small system with discrete energy levels connected to one or two superconducting leads. The superconductivity considered is conventional, described by the mean-field Barden-Cooper-Schrieffer (BCS) theory, and only a single electronic level is considered for the quantum dot. Nevertheless, the electrons on the dot (strongly) interact via Coulomb interaction. Even for a non-superconducting quantum dot, attached to a single reservoir, such interaction sets up the famous and difficult Kondo problem. Adding a second lead introduces the rich physics of quantum transport, and making the system superconducting means that the proximity and Josephson effects enter the picture, making the study of superconducting quantum dots a difficult problem on the intersections of many fields of physics.

This thesis is a purely theoretical study, however it is inspired by and related to the experiments on carbon-nanotube quantum dots performed in Laboratoire de physique des solides, Orsay, France. Both numerical and analytical results are used to obtain insights and formulas describing the system of the superconducting quantum dot.

Chapter 1 introduces the related concepts and physical background. Sec. 1.1 introduces the single-impurity Anderson model and the Kondo model for non-superconducting quantum dots. Sec. 1.2 introduces superconductivity, the Josephson effect, and the superconducting quantum point contact. Sec. 1.3 discusses some known theoretical results about the superconducting quantum dot (superconducting single-impurity Anderson model) itself, Sec. 1.4 deals with the nu-

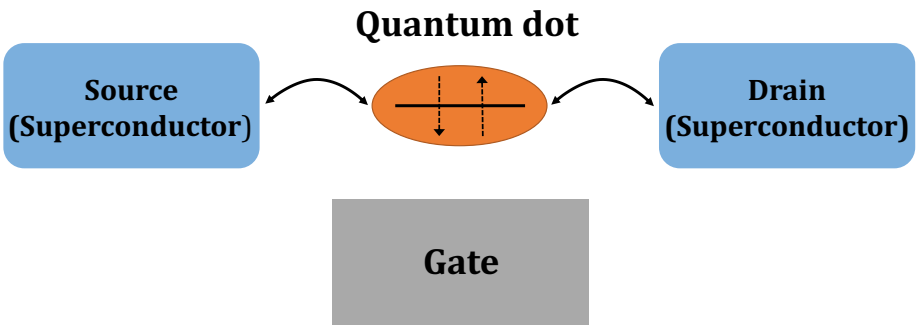

Figure 0.0.1: Schematic representation of a quantum dot connected to superconducting leads. Terminology reminiscent of a conventional field-effect transistor is often adopted.

merical renormalization group method, and Sec. 1.5 describes recent experiments on carbon nanotubes which have motivated our work.

Chapter 2 is a short summary of some results presented in the included articles, emphasizing my own contribution. Sec. 2.1 is based on Paper I and Paper II. It explains the influence of coupling asymmetry on the physics of a phase-biased superconducting quantum dot, finds the asymmetry of a specific experiment, and discusses to what extent the notion of Kondo universality is valid in the transport setup. Sec. 2.2 presents my contribution to interpreting the experimental AC Josephson measurement published in Paper III.

The research presented in this thesis is in line with the continued effort of the condensed matter theory group at KFKL MFF UK to fully understand the superconducting single-impurity Anderson model.

Chapter 1

Theoretical background

1.1 Non-superconducting quantum dots

In this thesis, by "quantum dot" we mean any system with discrete (though possibly degenerate) quantum levels. Examples of quantum dots include single atoms and molecules, impurities in bulk material and adatoms on surfaces, nanowires (e.g. InAs wires) and carbon nanotubes in certain regimes. (More about the spectrum of a carbon nanotube can be found in Sec. 1.1.5.) If the energy separation of levels of a quantum dot is large enough compared to other relevant energy scales of the system (Coulomb interaction, voltage bias, ...), it is possible to describe a single level and its interaction with the environment "locally" (in the energy-range of interest) via the single-impurity (or single-level) Anderson model.

1.1.1 Single-impurity Anderson model

The single-impurity Anderson model (SIAM) [1] has proven successful in description of dilute magnetic impurities in metals, adatoms on surfaces and quantum dots in the transport (source-drain-gate) setup. The Hamiltonian consists of a part describing the dot, the leads (or the bulk), and the tunnel-coupling between those two. For a quantum dot with a single spin-degenerate quantum level it reads

$$\mathcal{H} = \mathcal{H}_{\rm dot} + \sum_{\alpha}(\mathcal{H}^{\alpha}_{\rm lead} + \mathcal{H}^{\alpha}_{T}), \tag{1.1.1}$$

$$\mathcal{H}_{\rm dot} = \varepsilon \sum_{\sigma=\uparrow,\downarrow} d^{\dagger}_{\sigma} d_{\sigma} + U d^{\dagger}_{\uparrow} d_{\uparrow} d^{\dagger}_{\downarrow} d_{\downarrow} \tag{1.1.2}$$

$$\mathcal{H}^{\alpha}_{\rm lead} = \sum_{\mathbf{k}\sigma} \varepsilon_{\alpha\mathbf{k}}\, c^{\dagger}_{\alpha\mathbf{k}\sigma} c_{\alpha\mathbf{k}\sigma} \tag{1.1.3}$$

$$\mathcal{H}^{\alpha}_{T} = \sum_{\mathbf{k}\sigma} (t_{\alpha\mathbf{k}} c^{\dagger}_{\alpha\mathbf{k}\sigma} d_{\sigma} + \text{H.c.}) \tag{1.1.4}$$

where α numbers the lead(s) (e.g. $\alpha = L, R$ for left and right in the transport setup), $c^{\dagger}_{\alpha\mathbf{k}\sigma}$, $c_{\alpha\mathbf{k}\sigma}$ are the creation and annihilation operators of electrons in the leads with momentum $\mathbf{k}$ and spin σ and $d^{\dagger}_{\sigma}$ (d_{σ}) create (annihilate) on-dot electrons. The level-energy ε and the local Coulomb interaction U are the two

parameters which describe the dot. Tunneling matrix elements $t_{\alpha\mathbf{k}}$ give rise to tunnel-coupling magnitudes $\Gamma_\alpha(\varepsilon) \equiv \pi \sum_{\mathbf{k}} |t_{\alpha\mathbf{k}}|^2 \delta(\varepsilon - \varepsilon_{\alpha\mathbf{k}})$, which are assumed to be constant in the energy range of interest, $\Gamma_\alpha(\varepsilon) \simeq \Gamma_a$ (wide-band approximation). We define the total coupling as $\Gamma = \Gamma_R + \Gamma_L$.

For $\varepsilon = -\frac{U}{2}$ the Hamiltonian (1.1.1) is particle-hole symmetrical. This is also called half-filling.

The Γ quantity is best understood for the non-interacting ($U = 0$) Anderson model, sometimes also called the "resonant level". A well-known form of the (retarded, advanced) Green's function (see also Appendix A) of the non-interacting quantum dot at zero temperature reads [16]

$$G_0^{R,A}(\omega) = \frac{1}{\omega - \varepsilon \pm i\,\Gamma}\ , \tag{1.1.5}$$

independent of spin. This leads to a density of states (DOS) on the dot per spin

$$\rho_{d0} = \mp\frac{1}{\pi} Im\left\{G_0^{R,A}(\omega)\right\} = \frac{1}{\pi}\frac{\Gamma}{(\omega-\varepsilon)^2 + \Gamma^2}\ . \tag{1.1.6}$$

This broadened density of states on the dot stems entirely from the interaction or the resonant level with the leads, and $\Gamma = \Gamma_R + \Gamma_L$ is the half-width at half-maximum (HWHM) of the Lorentzian function[1]. The time scale $\hbar/\Gamma$ is the "lifetime" of the resonant level, or the time an electron spends on the dot.

For the interacting ($U \neq 0$) case, the dot's Green function acquires an additional self-energy term

$$G_\sigma^{R,A}(\omega) = \frac{1}{\omega - \varepsilon \pm i\,\Gamma - \Sigma_{U,\sigma}^{R,A}(\omega)} \tag{1.1.7}$$

which is not exactly known, and can be computed in various approximations. A logarithmic divergence in the third order of perturbation theory hints at the famous Kondo problem (see secs. 1.1.3, 1.1.4), an effect of strong correlations which is not captured at all in the mean-field approximation or in second-order perturbation theory.

1.1.2 Coulomb blockade physics

The basic transport setup consists of two lead electrons (the source and the drain, with chemical potentials μ_s, μ_d), coupled to the dot directly with $\Gamma_{R,L}$, and a gating electrode which is only capacitatively coupled to the quantum dot. Applying voltage to the gating electrode changes the position of the energy level(s) of the dot relative to $\mu_{s,d}$. Bias voltage, applied to the leads, changes the chemical potentials in the leads so that $eV = \mu_s - \mu_d$.

For weak tunnel coupling $\Gamma_{R,L}$ ($\Gamma \ll \Delta E$, where ΔE is the distance between consecutive energy levels of the dot, and $\Gamma \ll U$), electrons can only tunnel

[1]Sometimes, the relation $\Gamma_{R,L} = \pi\rho_{R,L}t_{R,L}^2$ is used. This is the simplest form of the wide-band approximation where $t_{\alpha\mathbf{k}}$ is considered fully $\mathbf{k}$-independent, $\Gamma_\alpha(\varepsilon) \equiv \pi \sum_{\mathbf{k}} |t_{\alpha\mathbf{k}}|^2 \delta(\varepsilon - \varepsilon_{\alpha\mathbf{k}}) \approx \pi t_\alpha^2 \sum_{\mathbf{k}} \delta(\varepsilon - \varepsilon_{\alpha\mathbf{k}})$. The density of states *of the lead electrons* $\rho_{R,L}$ is again counted per spin.

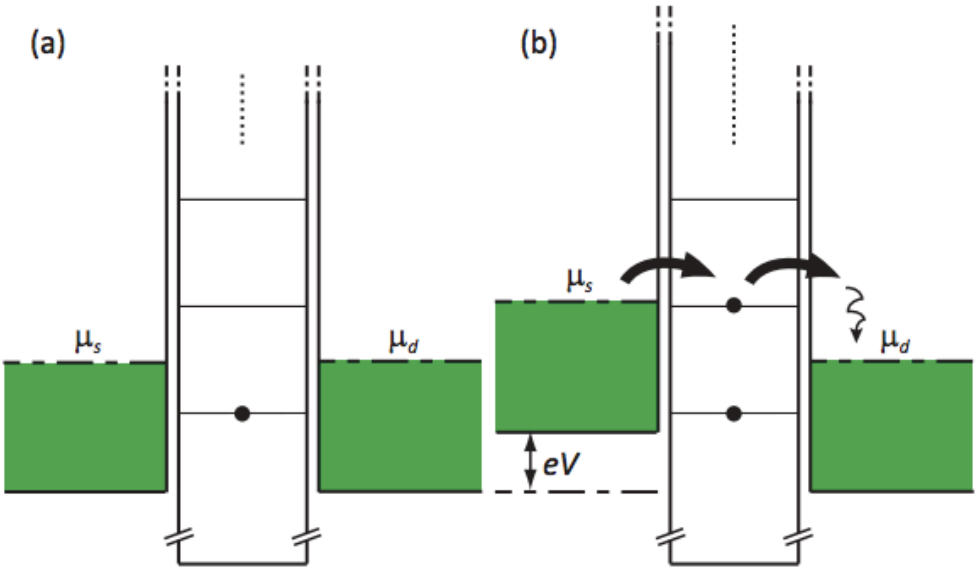

(a) (Figure source: [64]) The basic principle of the Coulomb blockade. (a) Because tunneling into the dot level would cost excess energy, single electron transport is blocked. (b) Under applied voltage bias, chemical potentials of the two leads differ. Electrons may tunnel through the junction freely if one of the dot levels is present in the gap between μ_s and μ_d. The position of the dot level(s) may be changed by gate-voltage.

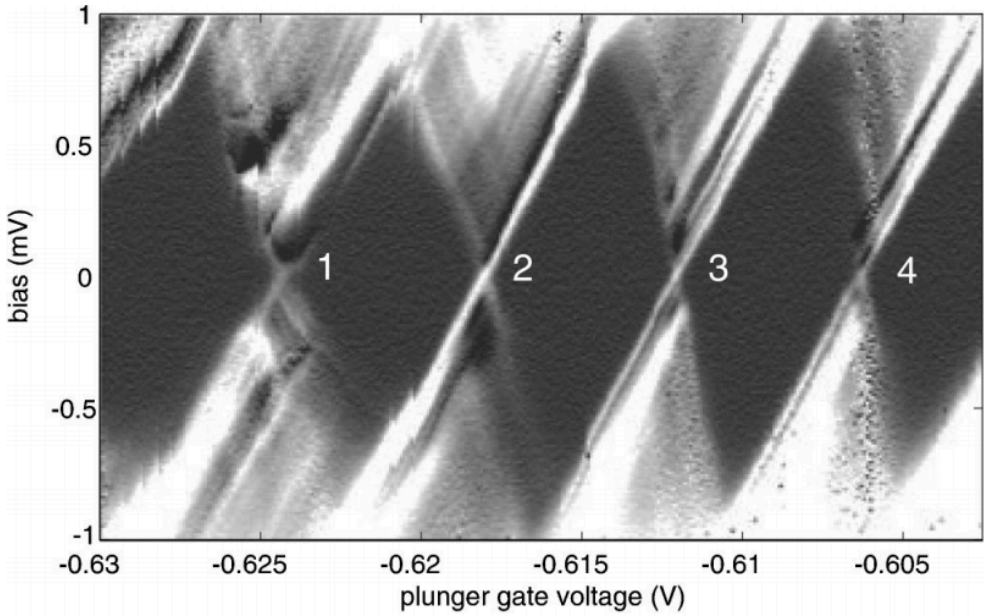

(b) (Figure source: [38]) Coulomb diamonds in a semiconductor quantum dot. The differential conductance as a function of gate voltage and bias voltage displays the typical pattern. In the dark areas, there is an average even occupation of the QD and transport is blocked.

Figure 1.1.1

through the barriers one by one. This is called sequential tunneling. In this regime, the occupation number of the dot is well defined, and current will flow from left to right only if there is an energy level of the QD between μ_s and μ_d. Fig. 1.1.1 shows a schematic of sequential tunneling, and the resulting "Coulomb diamond" pattern in differential conductance.

At higher temperatures, bias voltages or tunnel couplings Γ, two electrons can tunnel through the dot simultaneously (possibly borrowing energy for an intermediate virtual state). As most of this thesis is concerned with very low temperatures, these cotunneling processes are not of interest. However, what does play a role, is the Kondo effect.

1.1.3 The relation between Anderson and Kondo Hamiltonians

The Kondo model is a different model-description of a quantum impurity – describing a single spin (or a singly-occupied quantum level) coupled to a continuum of electrons. The Kondo model is described by the Hamiltonian

$$\mathcal{H}_K = \sum_k \varepsilon_k c_k^\dagger c_k - \sum_{kk'} J_{kk'} \mathbf{S}_d \cdot \mathbf{s}_{kk'} \tag{1.1.8}$$

with the spin operators

$$\mathbf{s}_{kk'} = \sum_{\sigma\sigma'} \frac{1}{2} c_{k\sigma}^\dagger \boldsymbol{\sigma}_{\sigma\sigma'} c_{k'\sigma'} \,, \quad \mathbf{S}_d = \sum_{\sigma\sigma'} \frac{1}{2} d_\sigma^\dagger \boldsymbol{\sigma}_{\sigma\sigma'} d_{\sigma'} \,, \tag{1.1.9}$$

where $\boldsymbol{\sigma}$ denote the Pauli matrices. In a certain range of parameters ensuring single occupation of the Anderson level ($\varepsilon/\Gamma \ll -1$, $(\varepsilon+U)/\Gamma \gg 1$), it is possible to transform the SIAM on the Kondo model via the so-called Schrieffer-Wolff transformation [59], as a result of a first-order perturbation expansion in the tunnel coupling $\mathcal{H}_T$. The Kondo coupling constant $J_{kk'}$ is identified as related to the parameters of the SIAM as

$$J_{k'k}^{SW} = t_{k'} t_k \left\{ \frac{1}{\varepsilon - \varepsilon_k} + \frac{1}{\varepsilon - \varepsilon_{k'}} - \frac{1}{\varepsilon + U - \varepsilon_k} - \frac{1}{\varepsilon + U - \varepsilon_{k'}} \right\} . \tag{1.1.10}$$

Making the assumption of k, k' momenta being close to the Fermi energy, one can neglect ε_k, $\varepsilon_{k'}$ in the denominators. Assuming $\Gamma = \pi\rho \left|t_{k_F}\right|^2$, equation (1.1.10) is simplified to

$$J\rho = \frac{2\Gamma}{\pi} \left(\frac{1}{\varepsilon} - \frac{1}{\varepsilon + U} \right), \tag{1.1.11}$$

where ρ is the density of states per spin in the bulk. This dimensionless quantity is used in expressions for the Kondo temperature in the next section.

1.1.4 The Kondo effect

The Kondo effect was first measured already in 1930's as an unexpected increase in electrical resistivity at low temperatures in metals (like copper and gold) with

added magnetic impurities (such as cobalt). It remained unexplained until the 1960's and 70's, when three nobel-prize laureates Jun Kondo, Philip W. Anderson and Kenneth G. Wilson contributed with their ideas, and continues to enjoy theoretical and experimental interest ever since. Interestingly enough, in quantum dots the same mechanisms which lead to the Kondo effect in aloys lead to an increase in *conductance*, not resistivity, at low temperatures (roughly) below the Kondo temperature T_K. While the resistance minimum in metals occurs around 10K, for single magnetic atoms between two leads the conductance minimum can be around 0.5 K [34]. For clean carbon nanotubes, a typical value of T_K is below 2K, and the conductance at low enough temperatures may approach the conductance quantum $2e^2/h$.

The Kondo-effect is caused by processes which flip the spin of the impurity. The graphical imagination often used in metals is that of a (large) impurity spin "screened" by conduction electrons. In quantum dots in the transport setup, a spin-flip process is the tunneling of an electron from one lead into the dot and (almost simultaneously) the dot-electron (with an opposite spin) tunneling out into the other lead. There is a resulting Kondo resonance visible in the spectral function and in conductance, which is always pinned to Fermi energy even though the dot's energy level ε is not.

The Kondo temperature in its precise meaning is an energy scale characterizing the temperature-dependence of conductance and other physical quantities. So called "Kondo universality" is this: As a function of T/T_K all temperature dependent curves look the same, although the underlying microscopic parameters may be very different. This is a remarkable property and a clear sign of Kondo physics, given that T_K can vary over several orders of magnitude. The Kondo temperature is an exponential function of J, and can be related to the parameters of the Anderson model [28] by

$$T_K \sim \sqrt{|\varepsilon(\varepsilon+U)\,J\rho|}\exp\left(1/J\rho\right), \tag{1.1.12}$$

with $J\rho = \frac{2\Gamma}{\pi}\left(\frac{1}{\varepsilon} - \frac{1}{\varepsilon+U}\right)$, see Eq. (1.1.11).

In half-filling ($\varepsilon = -U/2$), the exponent further simplifies to $J\rho = -\frac{8\Gamma}{\pi U}$ and the Kondo temperature becomes

$$T_K \sim \sqrt{\Gamma U/2}\exp\left(-\pi U/8\Gamma\right) \tag{1.1.13}$$

Numerical prefactors in Eqs. (1.1.12) and (1.1.13) may differ depending on the physical quantity we are interested in.[2]

In perturbation theory, spin-flip processes are third-order in the coupling J [6], and the corresponding term diverges logarithmically at low temperatures below T_K. This shows that perturbation expansions are unsuitable for quantitative results in the Kondo regime. Several numerical methods have been developed to deal with this effect of strong quantum correlations: In equilibrium (i.e. without voltage bias) the numerical renormalization group (NRG) method (Sec. 1.4) can

[2]Also note there is an alternative definition of T_K sometimes used in literature, in which Γ is twice as large, ie. corresponding to the full width at half maximum of the Kondo resonance. If mistaken, the factor of 2 in the exponent makes a significant difference.

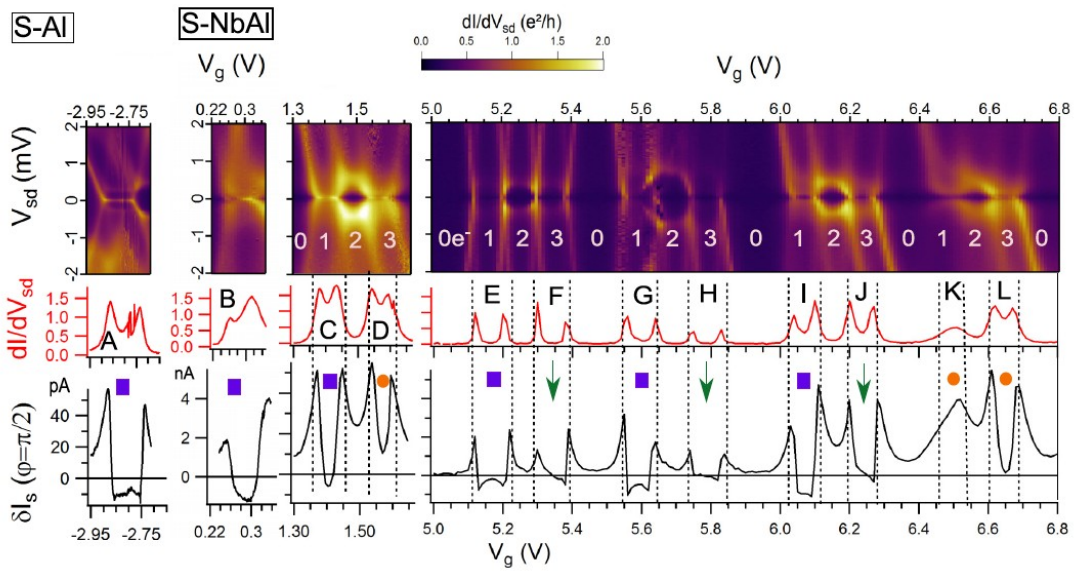

Figure 1.1.2: (Figure source: [21]) Differential conductance in a carbon-nanotube quantum dot in the normal (non-superconducting) state as a function of gate and bias voltage (upper panel), a cut of the same at zero bias (middle panel), and the supercurrent (lower panel). In the upper panel, we see Coulomb diamonds which have a periodicity of four, labeled by the number of electrons in their respective level. The diamond labeled "A" exhibits Kondo effect, which can be seen in the differential conductance as a line on zero bias voltage.

be used for quasiexact numerical results, at higher temperatures quantum Monte Carlo is available.

1.1.5 Carbon nanotube quantum dots

Single-wall carbon nanotubes (CNT) can be imagined as rolled up sheets of graphene. Valued for both their mechanical and electrical properties, they have become a field of study on their own, with review articles on transport properties including [11] and [35]. Without a superconducting lead, carbon nanotubes can be metallic or semiconducting. Provided the length of the nanotube is smaller than the mean free path of electrons, the CNT is a coherent lossless (ballistic) conductor. With low transparency of the contacts between the CNT and the leads, confinement in both the transversal and longitudinal dimensions leads to quantization, and the system becomes essentially zero-dimensional, a.k.a. a quantum dot. Very few (and often just one) energy levels are available for transport near the Fermi energy. In the first approximation, these energy levels are spaced apart ΔE (which is inversely proportional to the length of the CNT) and four-fold degenerate, namely in both spin and orbital quantum numbers (corresponding to electrons moving clockwise or counter-clockwise around the nanotube). In a clean CNT, the conductance of such a degenerate level reaches a maximal value of $G = \frac{4e^2}{h}$. The degeneracy is partially lifted by spin-orbit interactions or disorder into so-called Kramers' doublets separated by energy δE. If the levels of the CNT are well separated (Γ, $k_B T \ll U$, δE), the CNT quantum dot is in the

Coulomb blockade regime. The special electronic structure of a CNT leads to a specific structure of the Coulomb diamonds, with alternating larger and smaller diamonds depending on occupancy, which is well defined for low enough temperatures (see Fig. 1.1.2 and Refs. [19] for more detail). While a two-orbital model should be kept to describe all of the intricate physics in carbon nanotubes, for CNT's with $\Gamma \ll \delta E$, the single-impurity Anderson model can be also used and has been used with success eg. in Ref. [40, 43]. In oddly occupied diamonds, the Kondo effect as described in the previous section can develop[3].

[3]This is the SU(2) Kondo effect. Two-level phenomena, such as the SU(4) Kondo effect, will not be discussed in this thesis.

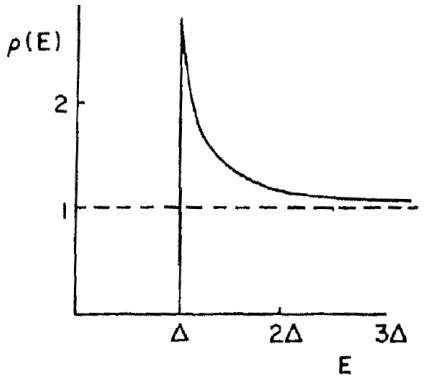

Figure 1.2.1: (Figure source: [41]) BCS density of states of a superconductor diverges at Δ and drops of as a square root. The DOS is particle-hole symmetrical and only states above the Fermi energy are shown.

1.2 Mesoscopic superconducting systems

Superconductivity in this thesis is conventional and treated in a standard way via the BCS theory (with "s-wave" pairing). The BCS theory in the bulk assumes a phonon-mediated attractive interaction between electrons, leading to the formation of Cooper pairs, which are responsible for the transport of the supercurrent, and to the opening of a gap Δ in the quasiparticle density of states (Fig. (1.2.1)).

A critical understanding when it comes to superconductors is, that the Cooper pairs overlap spatially and behave in a coherent way, and therefore the Cooper-pair condensate in one piece of a superconductor in equilibrium can be described by a single wavefunction (sometimes called the order parameter). Superconducting phenomena such as the Josephson effect (Sec. 1.2.2) depend on the variation of the phase of this wavefunction, or the phase-difference between two leads.

For superconducting nanostructures, the proximity effect (sometimes called boundary or Holm-Meissner effect) is also important. When a non-superconducting material (normal metal, quantum dot) is in close contact with a superconductor, an induced gap is opened in its density of states and it also becomes superconducting. This can be understood as leaking of Cooper pairs into the non-superconducting material, leading to a slow exponential drop-off of the order parameter at the boundary.

For good books on superconductivity see e.g. [18, 37, 65], for many-body descriptions of the BCS theory see also [6, 41].

1.2.1 The Hamiltonian of the superconducting lead

The BCS Hamiltonian, describing the interaction between Cooper pairs reads

$$\mathcal{H}_{\mathrm{BCS}} = \sum_{\mathbf{k}\sigma} \varepsilon_{\mathbf{k}} c^{\dagger}_{\mathbf{k}\sigma} c_{\mathbf{k}\sigma} + \sum_{\mathbf{k}\mathbf{k}'} V_{\mathbf{k}\mathbf{k}'} c^{\dagger}_{\mathbf{k}\uparrow} c^{\dagger}_{-\mathbf{k}\downarrow} c_{-\mathbf{k}'\downarrow} c_{\mathbf{k}'\uparrow} \tag{1.2.1}$$

where the coupling strength $V_{\mathbf{k}\mathbf{k}'}$ is a negative constant for $|\varepsilon_{\mathbf{k}}|, |\varepsilon_{\mathbf{k}'}|$ below the Debye energy and zero otherwise. This Hamiltonian is treated in a mean-field way [6], obtaining

$$\mathcal{H}_{\mathrm{BCS}}^{\mathrm{MF}} = \sum_{\mathbf{k}\sigma} \varepsilon_{\mathbf{k}} c_{\mathbf{k}\sigma}^{\dagger} c_{\mathbf{k}\sigma} - \sum_{\mathbf{k}} \left(\mathbf{\Delta}_{\mathbf{k}} c_{\mathbf{k}\uparrow}^{\dagger} c_{-\mathbf{k}\downarrow}^{\dagger} + \mathbf{\Delta}_{\mathbf{k}}^{*} c_{-\mathbf{k}\downarrow} c_{\mathbf{k}\uparrow} \right) \tag{1.2.2}$$

with a generally complex order parameter

$$\mathbf{\Delta}_{\mathbf{k}} = -\sum_{\mathbf{k}\mathbf{k}'} V_{\mathbf{k}\mathbf{k}'} \left\langle c_{-\mathbf{k}'\downarrow} c_{\mathbf{k}'\uparrow} \right\rangle . \tag{1.2.3}$$

Assuming $V_{\mathbf{k}\mathbf{k}'}$ constant in a certain range of $|\mathbf{k}|$'s around the Fermi energy and zero otherwise, in that range, $\mathbf{\Delta}_{\mathbf{k}}$ is $\mathbf{k}$- independent and the subscript can be dropped. Denoting Δ_α the amplitude of (1.2.3) in a material and φ_α it's phase, we get the well known form of the BCS Hamiltonian for a superconducting lead

$$\mathcal{H}_{\mathrm{lead}} = \sum_{\mathbf{k}\sigma} \varepsilon_{\mathbf{k}} c_{\mathbf{k}\sigma}^{\dagger} c_{\mathbf{k}\sigma} - \Delta_\alpha \sum_{\mathbf{k}} \left(e^{i\varphi_\alpha} c_{\mathbf{k}\uparrow}^{\dagger} c_{-\mathbf{k}\downarrow}^{\dagger} + e^{-i\varphi_\alpha} c_{-\mathbf{k}\downarrow} c_{\mathbf{k}\uparrow} \right) , \tag{1.2.4}$$

The lead Hamiltonian (1.2.4) is used throughout this thesis, see Sec. 1.3.1 for the full Hamiltonian of the S-QD-S system.

1.2.2 DC and AC Josephson effect

The Josephson effect refers to supercurrent flowing through a thin non-superconducting layer between two superconductors (a Josephson junction). It is, at its basis, a phenomenon of quantum tunneling. Given a difference in the overall phases of the two superconductors (from now on always denoted φ), there can be supercurrent with no bias voltage applied. The first Josephson relation for a planar tunnel junction

$$\mathcal{J}(\varphi) = \mathcal{J}_c \sin\varphi \tag{1.2.5}$$

connects the supercurrent $\mathcal{J}$ and the phase difference φ. The critical current $\mathcal{J}_c$ is a constant which depends on the exact geometry of the junction. Eq. (1.2.5) is valid in the absence of any voltage bias, and in case of a constant φ leads to a constant supercurrent, thus the name DC Josephson effect. The suppercurrent is dissipation-less, yet potential energy $U_s = E_c(1 - \cos\varphi)$ with $E_c = \hbar\mathcal{J}_c/2e$ is bound in the junction [65].

Eq. (1.2.5) is an example of what we call a current-phase relation (CPR). The CPR may be non-sinusoidal for structures more complicated then a simple Josephson junction (namely for the superconducting quantum dot near the $0-\pi$ transition, see Sec. (1.3.4)).

If a constant bias voltage V is applied across a junction, the so called AC Josephson effect leads to an alternating current, generated by a changing phase difference which obeys

$$\frac{d\varphi}{dt} = \frac{2eV}{\hbar} . \tag{1.2.6}$$

Josephson relations (1.2.5) and (1.2.6), first published in 1962, have become the basis of a rich field of mesoscopic superconducting physics.

1.2.3 Superconducting quantum point contact

One special case of a Josephson junction, which has been extensively studied (notably [5, 2, 15, 52]) is the superconducting quantum point contact (QPC). By that we understand a point-like constriction, which is both short - shorter than the coherence length of Cooper pairs in the superconductor - and narrow (as opposed to the spatially wide layer of a classical Josephson junction). The transverse directions need to be comparable to the Fermi wavelength for the transverse modes to be quantized, which leads to a quantized conductance, and a quantized supercurrent, which is independent of the exact geometry of the junction.

The superconducting quantum point contact is in some features similar to the superconducting quantum dot, the main topic of this thesis, but can be treated as a non-interacting problem (due to the absence of the Coulomb interaction). Ref. [5] uses the Bogoljubov-de-Gennes equation and the WKB equation with appropriate boundary condition to find the band structure and the quantized DC supercurrent. Summarizing some results, the band-structure of the superconducting QPC has been found to have a continuum of states above Δ (and below $-\Delta$), and two discrete subgap states (sometimes called Andreev bound states, ABS) of energy $E_\pm = \pm\Delta\sqrt{1 - D\sin^2\frac{\varphi}{2}}$, where D is the transmission the very same QPC would have without superconductivity. In the quantum point contact, these subgap states carry the supercurrent (surprisingly, the contribution of the continuum can be neglected). Moreover, the amplitude of the stationary (V=0) supercurrent can be found as a derivative of the occupied subgap state $\mathcal{J}(\varphi) = \frac{2e}{\hbar}\frac{dE_-(\varphi)}{d\varphi}$, yielding the stationary current-phase relation for a single transport channel

$$\mathcal{J}(\varphi) = \frac{eD\Delta}{2\hbar}\frac{\sin\varphi}{\sqrt{1 - D\sin^2\frac{\varphi}{2}}}. \tag{1.2.7}$$

This current-phase relation is very different from Eq. (1.2.5). In particular, for perfect transmission $D = 1$, Eq. (1.2.7) reduces to $\mathcal{J}(\varphi) = \frac{e\Delta}{\hbar}\sin\left(\frac{\varphi}{2}\right)\operatorname{sgn}\left(\cos\left(\frac{\varphi}{2}\right)\right)$.

The AC Josephson effect has been also studied. Ref. [2] uses the scattering S-matrix approach to find the components of the AC Josephson current in a junction with non-zero reflectivity, while Ref. [15] uses non-equilibrium Green's function approach to the same problem, and numerical results for the first Fourier components of the supercurrent are available for different reflectivities (to be used in Sec. 2.2.4).

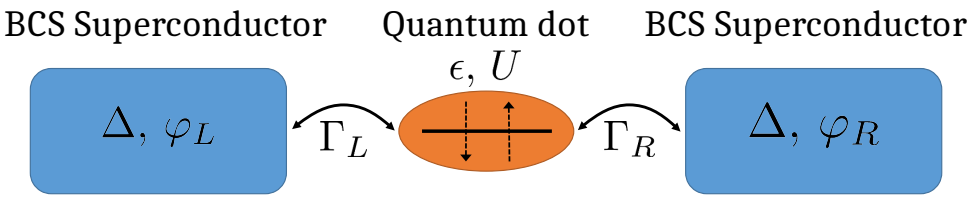

Figure 1.3.1: Schematic of the superconducting quantum dot with parameter description.

1.3 Superconducting quantum dots

We now turn our attention to the core topic of this thesis: A single-level quantum dot connected to BCS superconducting leads, with (strong) Coulomb interaction between electrons. This is a special kind of Josephson junction, as well as a special setup for the (already difficult to solve) problem of a quantum dot with interaction coupled to two leads, which we talked about in Sec. 1.1. While this system has been studied since the nineties (review articles include [17, 42, 44]), once strong interaction enters, questions have remained open and the only way to get exact quantitative results are still numerical methods.

With the introduction of superconductivity into the SIAM, several new phenomena emerge. The superconducting proximity effect induces a gap in the local density of stated on the quantum dot at the Fermi level. This gap is, in the appropriate parameter range, said to be "in competition" with the Kondo resonance we expect in non-superconducting systems. As in the case of the superconducting quantum point contact, subgap states are present. Unlike the QPC though, these can cross, which leads to a (first-order) quantum phase transition at zero temperature, usually called the $0-\pi$ transition. This phase transition can be induced by changing the parameters of the QD, including ε and φ as demonstrated by experiments (see e.g. [66, 31] for demonstration of a gate-controlled $0-\pi$ transition, and [20, 21] for phase control), and is accompanied by a sudden change in the amplitude of the supercurrent. This makes the superconducting quantum dot interesting as possible switching elements for superconducting electronics.

In BCS theory, charge-conservation is broken. One of the effects is, that NRG calculations are an order of magnitude more computationally demanding in comparison to the non-superconducting metal-impurity system. Part of the effort of our theory group and my thesis has been to find fast yet still reliable methods to characterize the dot, decreasing the need for heavy numerics.

This chapter will introduce the superconducting version of the single-impurity Anderson model and the (non-interacting) Green's function of the dot in Nambu formalism (Sec. 1.3.1), the subgap states and the $0-\pi$ transition in an "atomic limit" view for simplified understanding (Sec. 1.3.2), and finally the phase diagram and the interplay between Kondo physics and superconductivity is presented (Sec. 1.3.4).

1.3.1 Superconducting single-impurity Anderson model

The superconducting single-impurity Anderson model (sc-SIAM) for the quantum dot attached to superconducting leads is the same as presented in Sec. (1.1.1) with the exception of the lead Hamiltonian (1.1.3) now being changed according to Eq. 1.2.4:

$$\mathcal{H} = \mathcal{H}_{\rm dot} + \sum_{\alpha}(\mathcal{H}^{\alpha}_{\rm lead} + \mathcal{H}^{\alpha}_{T}), \tag{1.3.1}$$

$$\mathcal{H}_{\rm dot} = \varepsilon \sum_{\sigma=\uparrow,\downarrow} d^{\dagger}_{\sigma} d_{\sigma} + U d^{\dagger}_{\uparrow} d_{\uparrow} d^{\dagger}_{\downarrow} d_{\downarrow} \tag{1.3.2}$$

$$\mathcal{H}^{\alpha}_{\rm lead} = \sum_{\mathbf{k}\sigma} \varepsilon_{\alpha\mathbf{k}}\, c^{\dagger}_{\alpha\mathbf{k}\sigma} c_{\alpha\mathbf{k}\sigma} - \Delta_{\alpha} \sum_{\mathbf{k}} (e^{i\varphi_{\alpha}} c^{\dagger}_{\alpha\mathbf{k}\uparrow} c^{\dagger}_{\alpha\,-\mathbf{k}\downarrow} + \text{H.c.}) \tag{1.3.3}$$

$$\mathcal{H}^{\alpha}_{T} = \sum_{\mathbf{k}\sigma} (t_{\alpha\mathbf{k}} c^{\dagger}_{\alpha\mathbf{k}\sigma} d_{\sigma} + \text{H.c.}) \tag{1.3.4}$$

with $\alpha = L, R$ again denoting the left and right lead. The added term is the standard BCS Hamiltonian, with $\Delta_{\alpha} e^{i\varphi_{\alpha}}$ being the superconducting order parameter. As in the previous sections, $\varphi \equiv \varphi_L - \varphi_R$ is the superconducting phase difference, and the tunnel coupling $\Gamma_{\alpha} \simeq \Gamma_{\alpha}(\varepsilon) \equiv \pi \sum_{\mathbf{k}} |t_{\alpha\mathbf{k}}|^2 \delta(\varepsilon - \varepsilon_{\alpha}(\mathbf{k}))$ is assumed to be constant in the energy range of interest. The coupling asymmetry a is defined as $a = \Gamma_L/\Gamma_R$. Throughout this thesis, I consider the left and right lead to have the same amplitude of the gap, $\Delta = \Delta_L = \Delta_R$.

The Matsubara Green's function of the quantum dot is a 2×2 matrix in the Nambu spinor formalism (see Appendix A for the Matsubara formalism and Appendix B for the Nambu representation)

$$\widehat{G}(\tau) = \begin{pmatrix} G(\tau) & \mathcal{G}(\tau) \\ \bar{\mathcal{G}}(\tau) & \bar{G}(\tau) \end{pmatrix} = -\begin{pmatrix} \langle T_{\tau}[d_{\uparrow}(\tau) d^{\dagger}_{\uparrow}(0)]\rangle\ , & \langle T_{\tau}[d_{\uparrow}(\tau) d_{\downarrow}(0)]\rangle \\ \langle T_{\tau}[d^{\dagger}_{\downarrow}(\tau) d^{\dagger}_{\uparrow}(0)]\rangle\ , & \langle T_{\tau}[d^{\dagger}_{\downarrow}(\tau) d_{\downarrow}(0)]\rangle \end{pmatrix} \tag{1.3.5}$$

The exact form of the non-interacting ($U = 0$) Green's function $\widehat{G}_0(i\omega_n)$ can be written as a function of Matsubara frequencies $\omega_n \equiv (2n+1)\pi/\beta$ (the derivation of $\widehat{G}_0$ is given in Appendix B):

$$\widehat{G}_0(i\omega_n) = \begin{pmatrix} i\omega_n[1 + s(i\omega_n)] - \varepsilon\ , & \Delta_{\varphi}(i\omega_n) \\ \Delta^{*}_{\varphi}(i\omega_n)\ , & i\omega_n[1 + s(i\omega_n)] + \varepsilon \end{pmatrix}^{-1}, \tag{1.3.6}$$

where

$$s(i\omega_n) = \sum_{\alpha=L,R} \frac{\Gamma_{\alpha}}{\sqrt{\Delta^2_{\alpha} + \omega^2_n}} \tag{1.3.7}$$

is a hybridization term which is due to the coupling to the leads, and

$$\Delta_{\varphi}(i\omega_n) = \sum_{\alpha=L,R} \frac{\Gamma_{\alpha}\Delta_{\alpha}}{\sqrt{\Delta^2_{\alpha} + \omega^2_n}} e^{i\varphi_{\alpha}} \tag{1.3.8}$$

is the off-diagonal element of $\widehat{G}_0$ which contains the dependence on the superconducting phase-difference. The non-interacting Green's function $\hat{G}_0$ is taken as a starting point for the derivation of our symmetry-asymmetry relation (Sec. 2.1.1, Paper I).

The full Green's function $\widehat{G}^{-1}(i\omega_n) = \widehat{G}_0^{-1}(i\omega_n) - \widehat{\Sigma}(i\omega_n)$ contains additional self-energy terms, which are not known exactly. Its second-order perturbative treatment is given in Refs. [78, 79], and is interestingly more successful for the superconducting quantum dot (up to approx. $U/\Gamma \approx 6$, before strongly correlated Kondo physics becomes dominant) than its normal-state counterpart. Numerical renormalization group solutions are considered quasi-exact for the equilibrium setup.

1.3.2 The atomic limit

Some basic properties of the superconducting quantum can be understood in the so-called atomic limit (see Refs. [32, 45, 50]). This refers to solving the interacting $U \neq 0$ sc-SIAM model with the assumption $\Delta \to \infty$. It is the only limit of the interacting model, which can be solved analytically, providing some insight into the structure of the lowest lying many-body eigenstates and revealing a quantum phase transition.

For $\Gamma_R = \Gamma_L$ and $\Delta \to \infty$ the non-interacting Green's function (1.3.6) takes the form

$$\widehat{G}_0^{\mathrm{AL}}(i\omega_n) = \begin{pmatrix} i\omega_n - \varepsilon & \Delta_d(\varphi) \\ \Delta_d(\varphi) & i\omega_n + \varepsilon \end{pmatrix}^{-1} = \frac{1}{i\omega_n - H_0^{\mathrm{AL}}} \tag{1.3.9}$$

with $\Delta_d(\varphi) = \Gamma \cos\frac{\varphi}{2}$ and $H_0^{\mathrm{AL}} = \varepsilon \sum_{\sigma=\uparrow,\downarrow} d_\sigma^\dagger d_\sigma - \Delta_d(\varphi)\left(d_\uparrow^\dagger d_\downarrow^\dagger + d_\downarrow d_\uparrow\right)$, which is ω_n independent. The interaction term may be simply added

$$H^{\mathrm{AL}} = \varepsilon \sum_{\sigma=\uparrow,\downarrow} d_\sigma^\dagger d_\sigma - \Delta_d(\varphi)\left(d_\uparrow^\dagger d_\downarrow^\dagger + d_\downarrow d_\uparrow\right) + U n_{d\uparrow} n_{d\downarrow}. \tag{1.3.10}$$

This Hamiltonian can written in the basis $|0\rangle, |\uparrow\rangle, |\downarrow\rangle, |\uparrow\downarrow\rangle$ and diagonalized. We obtain doubly degenerate eigenenergy ε belonging to the $|\uparrow\rangle$ and $|\downarrow\rangle$ states, and eigenenergies $E_\pm = \left(\frac{U}{2} + \varepsilon\right) \pm \sqrt{\left(\frac{U}{2} + \varepsilon\right)^2 + \Delta_d^2}$ belonging to a combination of $|\uparrow\downarrow\rangle$ and $|0\rangle$ states. (Note that it still makes sense to speak about even and odd occupation of eigenstates, yet the distinction between an empty and a doubly occupied dot is lost.) The ground state is non-degenerate (singlet) for $E_- < \varepsilon$ and twofold spin-degenerate (doublet) otherwise, exposing a first-order impurity quantum phase transition with the phase boundary given by

$$\left(\frac{U}{2} + \varepsilon\right)^2 + \Gamma^2 \cos^2\left(\frac{\varphi}{2}\right) = \left(\frac{U}{2}\right)^2, \tag{1.3.11}$$

a semi-ellipse in the $\varepsilon - \Gamma$ parameter space. The expressions for the eigenenergies and the phase-boundary further simplify for half-filling ($\varepsilon = -\frac{U}{2}$).

Qualitatively, this description shows some of the main features of the sc-SIAM. In the full model, the ground state is also either a singlet or a doublet, and once interaction is in the picture, a quantum phase-transition (called $0-\pi$ after the change in the phase-dependence, and thus the sign of the supercurrent) is possible. Note that the gap Δ doesn't tend to be the biggest energy scale in experiment - quite on the contrary, it is possible for U and Γ to be larger than Δ by an order of magnitude, so the results of the atomic limit can't give quantitative predictions.

1.3.3 Approximate methods vs. numerically demanding quasiexact approaches

The full Hamiltonian of the sc-SIAM (1.3.1) cannot be diagonalized analytically, but various approximations and numerical methods have been applied. Here I give a brief overview, see review [44] for more detail.

Already the 1973 study of a classical magnetic moment in a superconductor [60] indicates a crossing of subgap states, and the approximate treatment of a Kondo impurity by Glazman and Matveev [25] in 1989 hints a change in sign of the supercurrent, and thus a phase-transition. A mean-field approach to the sc-SIAM, if applied naively, suggests spin symmetry breaking, but this is an artifact of the method [44]. With more success, perturbation expansions in Γ have been attempted [49, 26] (yielding results with limited validity for $k_B T \gg \Gamma$), as well as perturbative expansions around the atomic limit [46]. For small and intermediate Coulomb interaction ($U/\Gamma \leq 8$ in half-filling) second-order perturbation theories are effective [68, 78, 79], and have been even attempted out of equilibrium [22]. A successful semi-analytical method is also the functional renormalization group [32, 47].

The most exact results can be gained by computationally demanding numerical methods, namely the numerical renormalization group (NRG), which is best suited for zero (or close to zero) temperature, and finite-temperature quantum Monte Carlo (QMC)[4]. The NRG has been first applied to the Kondo problem in a superconductor in 1992, Refs. [57, 56], later came the sc-SIAM with $\varphi = 0$ (effectively one lead), Ref. [72]. In 2004, the full two-lead transport setup (which is more demanding of computational resources) has been studied by both NRG [12] and QMC [61, 62, 13, 63]. The results for the Josephson current in these early studies didn't agree, and the dispute has been clarified by a later NRG study [32], and more reliable QMC data have been published eg. in Ref. [39]. Since then, both NRG and QMC have been successfully used to describe experimental findings (see Sec. 1.5 for chosen experimental references). Finite-temperature NRG and QMC calculations have been also directly compared in Ref. [55] and our Paper II, and satisfactory agreement has been found.

1.3.4 Subgap states and the phase diagram of a superconducting quantum dot

In this subsection I describe some basic properties of the sc-SIAM as known from previous research - the spectrum and the phase diagram.

The many-body spectrum. Setting the energy of the ground-state to zero, the many-body spectrum of the sc-SIAM - eigenenergies of the full Hamiltonian (1.3.1) - exhibits a continuum of eigenenergies above Δ (similarly to the quantum point contact) and one or two discrete excited states inside the gap.[5] As we have

[4] In fact, multiple variants of the QMC method have been used, yet this is outside the scope of this thesis.

[5] The energies of the subgap states can (in principle) be computed from the determinant of the exact inverse Green's function (more accurately, from its continuation to the real axis)

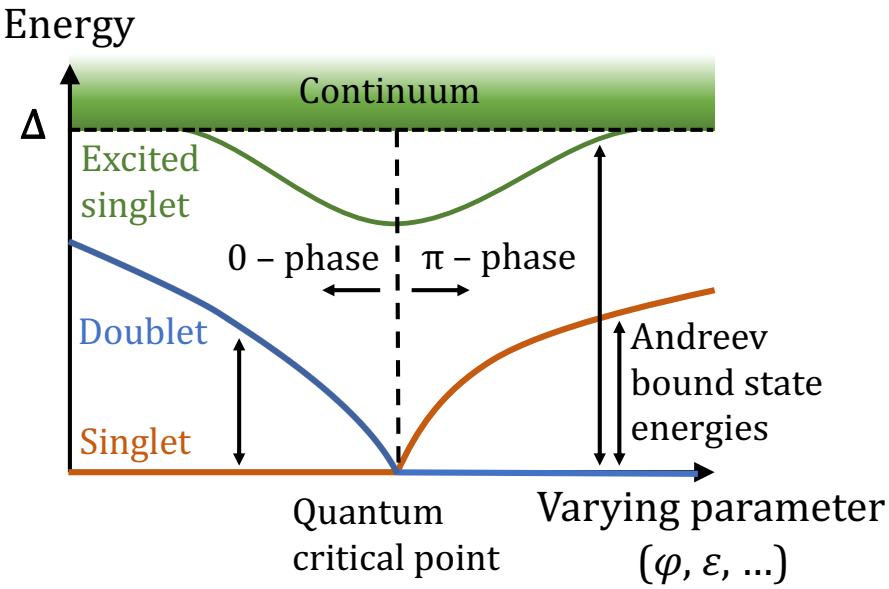

Figure 1.3.2: Scheme of many-body eigenstates of the superconducting quantum dot. The energy of the ground state has been set to zero. The crossing of eigenstates marks the $0-\pi$ impurity quantum phase transition. The energies of Andreev bound states are given by single-particle jumps between the ground state and excited states with different spin parity.

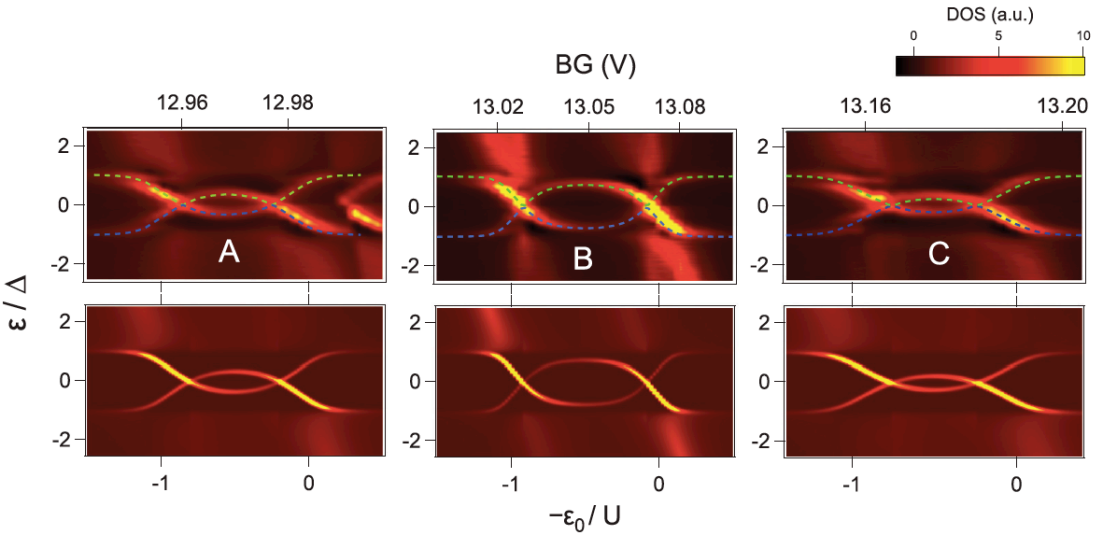

Figure 1.3.3: (Figure source: [53]) Experimental data for the tunneling density of states in a CNT quantum dot as a function of gate-voltage (top) and a pair of Andreev bound state energies obtained by NRG for fixed U/Δ ratios and Γ as a the only fitting parameter (bottom).

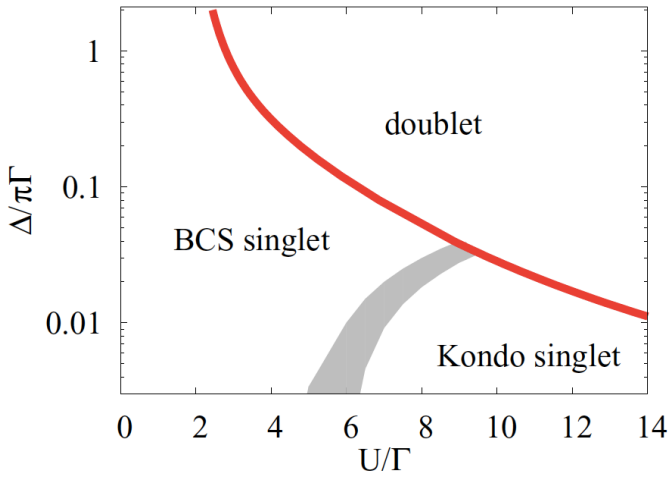

Figure 1.3.4: (Figure source: [79]) Phase diagram of the superconducting quantum dot in half-filling $\varepsilon = -U/2$ and $\varphi = 0$. The $0-$phase has a singlet ground state, while the $\pi-$phase has a spin doublet ground state. With changing interaction strength, the singlet gradually changes its character from BCS-like to Kondo-like. The grey transition region has been estimated as the area where second-order perturbation theory fails [79].

seen in the atomic limit, the ground state and the first excited state can be either a spin singlet (S) or a doublet (D), while the second excited state is always a singlet (ES). The excited singlet may merge with the continuum of states above Δ. (See Fig. 1.3.2.)

Andreev bound states. Confusion often arises between the many-body eigenstates of the Hamiltonian, and so-called Andreev bound states[6], which are single-particle states observed in the spectral function and in tunneling experiments. The ABS can be understood as arising from transitions between the lowest excited many-body states and the ground state, and one transition gives rise to a *pair* of ABS at $\pm E_A$ around the Fermi energy. The transitions (imagine single-electron jumps) occur between states with different spin parity, a transition between the two singlet states is impossible.

The $0-\pi$ transition The crossing of ABS corresponds to the underlying crossing of the many-body singlet and doublet states and marks the quantum critical point, a first-order impurity quantum phase transition commonly called $0-\pi$. With a non-zero interaction strength U, a change in any of the model

being zero.

[6]The terms "Andreev reflection" and "Andreev bound state" originally refer to superconductor-metal (S-N) interfaces and S-N-S junctions. At the N-S interface, an electron is supposed to be Andreev-reflected in a charge- and momentum-conserving way, forming an electron-hole pair in the metal and a Cooper pair in the superconductor. The case of the quantum dot (or point contact) doesn't necessarily fit this simple physical picture. Another, equally inaccurate, name sometimes used for the subgap states in a quantum dot is Yu-Shiba-Rusinov, or just "Shiba", states, which originally refers to subgap states generated by a *classical* magnetic moment in a superconductor.

parameters ε, φ, Γ and even the asymmetry a can cause the phase-transition [79].

The $0-\pi$ transition gets its name after the change in the current-phase relation: In the 0-phase, unless very close to the transition point, the CPR of the quantum dot is close to sinusoidal, while in the π-phase the supercurrent has the opposite sign (its phase shifted by π) and a smaller amplitude. Zero-temperature methods, like the NRG, show a sharp jump in the CPR, while at realistic temperatures, there is more of a smooth crossover (see also Sec. 1.5.1, Fig. 1.5.2).

For the two different phases of the quantum dot, the structure of the subgap states is as follows:

- In the 0-phase the ground state is a singlet with energy E_S. A spin-degenerate doublet with energy E_D is the first excited state, and possibly a the second excited singlet with energy E_{ES} may be present inside the gap. Only one pair of ABS with energy $E_\mathrm{A} = E_D - E_S$ is visible in the spectral function. As long at the quantum dot stays in the 0-phase, the spectrum is very similar to the quantum point contact.

- In the π-phase, the spin doublet is the ground state. Since the ground state has a different spin parity than both excited states, one or two pairs of ABS with energies $E_\mathrm{A}^{(1)} = E_S - E_D$ and $E_\mathrm{A}^{(2)} = E_{ES} - E_D$ may be visible in the gap, depending on parameters.

The "Kondo regime" of the quantum dot. In Sec. 1.1 we have talked about the Kondo effect in quantum dots, the universality property of the Kondo Hamiltonian, and the possibility to map the SIAM and the Kondo models in a suitable parameter regime (i.e. $U/\Gamma \gg 1$ for half-filling). It is a-priori not clear at all, that the Kondo effect survives in the presence of superconductivity - both the Kondo resonance and the superconducting gap occur at the Fermi level. It has been shown for quantum impurities in superconductors (e.g. in Ref. [72] by NRG, and in Ref. [8] experimentally) that for a small enough superconducting gap in comparison to the Kondo temperature (Eq. (1.1.12)), $\Delta \ll T_K$, the quantum dot keeps Kondo-like universality. We discuss how this is influenced by coupling asymmetry in Paper II and in Sec. 2.1.3 of this thesis.

The range of parameters where Kondo behavior is expected is commonly called the Kondo regime, even if no Kondo physics can take place in the $\pi-$phase. We want to stress that, while Δ/T_K comparisons are popular, outside of the Kondo regime the T_K scale is meaningless for the SIAM.

The phase diagram. The phase diagram of the quantum dot in the $\Delta - U$ plane (with fixed $\varphi = 0$ and $\varepsilon = -U/2$) is shown in Fig. 1.3.4. The $\pi-$phase with its doubly degenerate ground state emerges for large enough Coulomb interaction U. In the $0-$phase, while the structure of many-body states remains the same, the singlet ground state smoothly changes its character. For large U/Γ and $T_K \gg \Delta$, the ground state is Kondo-like, while for small U/Γ, BCS superconductivity is the main physical mechanism.

1.4 The numerical renormalization group method

The idea of renormalization (also used in high-energy physics and for historical reasons inaccurately called "group") is to, step by step, integrate out high-energy (short wavelength) degrees of freedom. Each iteration of the procedure must reproduce the functional form of the theory (represented by the Hamiltonian or the action functional), only changing the coupling constants. With enough iterations, it is eventually possible to get a solution, i.e. a fixed point of the renormalization mapping. The application to condensed matter problems has it's own specifics.

The numerical renormalization group is a method of solving strongly interacting quantum impurity problems. It was invented in the 1970's by Kenneth Wilson (Nobel prize laureate in 1982) to solve the Kondo problem [70], and further adapted to more complicated quantum impurity setups (see [9] for a review). While involving approximations, the procedure is non-perturbative in any of the system's parameters. This is necessary due to vastly different energy scales inherent to quantum impurity problems (remember the exponentially thin Kondo resonance in the SIAM).

The basic setup of the NRG calculation is a small system (the impurity) coupled to a "bath" or conduction band (the lead, represented by non-interacting or superconducting electrons), as sketched in Fig. 1.4.1a. The bandwidth of the conduction band in energy is denoted D[7]. The energy-dependent coupling of the impurity to the bath is described by the hybridization function, which for the SIAM is the energy-dependent tunnel coupling magnitude $\Gamma(\omega) = \pi \sum_k t_{\mathbf{k}}^2 \delta(\omega - \varepsilon_k)$[8] known from Sec. 1.1.1. The hybridization function is assumed to be non-zero only within the conduction band $[-D, D]$.

The NRG calculation consists of a few steps (following Ref. [9], see also Fig. 1.4.1):

1. Dividing the conduction band into a set of intervals of exponentially decreasing length separated by points $\pm\Lambda^{-n}$. The choice of the discretization parameter Λ contributes to the precision of further approximations. The "logarithmic discretization" is chosen to capture effects close to the Fermi energy with enough precision.

2. Discretizing the hybridization function, so that it is replaced by only one value in each of the above-mentioned intervals. This is an approximation, and it's precision is not a priori clear. The limit $\Lambda \to 1$ should recover the precise model, and it turns out, that $\Lambda = 2$ for the non-superconducting SIAM and $\Lambda = 4$ for sc-SIAM often lead to good enough results.

[7] The bandwidth D is the largest energy scale in NRG. It's usual to count all other energy scales "in units of the bandwidth".

[8] The hybridization function is denoted $\Delta(\omega)$ in Fig. 1.4.1a-b, as usual for non-superconducting systems. In the text I stick to $\Gamma(\omega)$ to avoid confusion with the superconducting gap Δ. Also, coupling constants $t_{\mathbf{k}}$ in $\Gamma(\omega) = \pi \sum_k t_{\mathbf{k}}^2 \delta(\omega - \varepsilon_k)$ are not to be confused with the hopping elements of the chain Hamiltonian t_n in Fig. 1.4.1c.

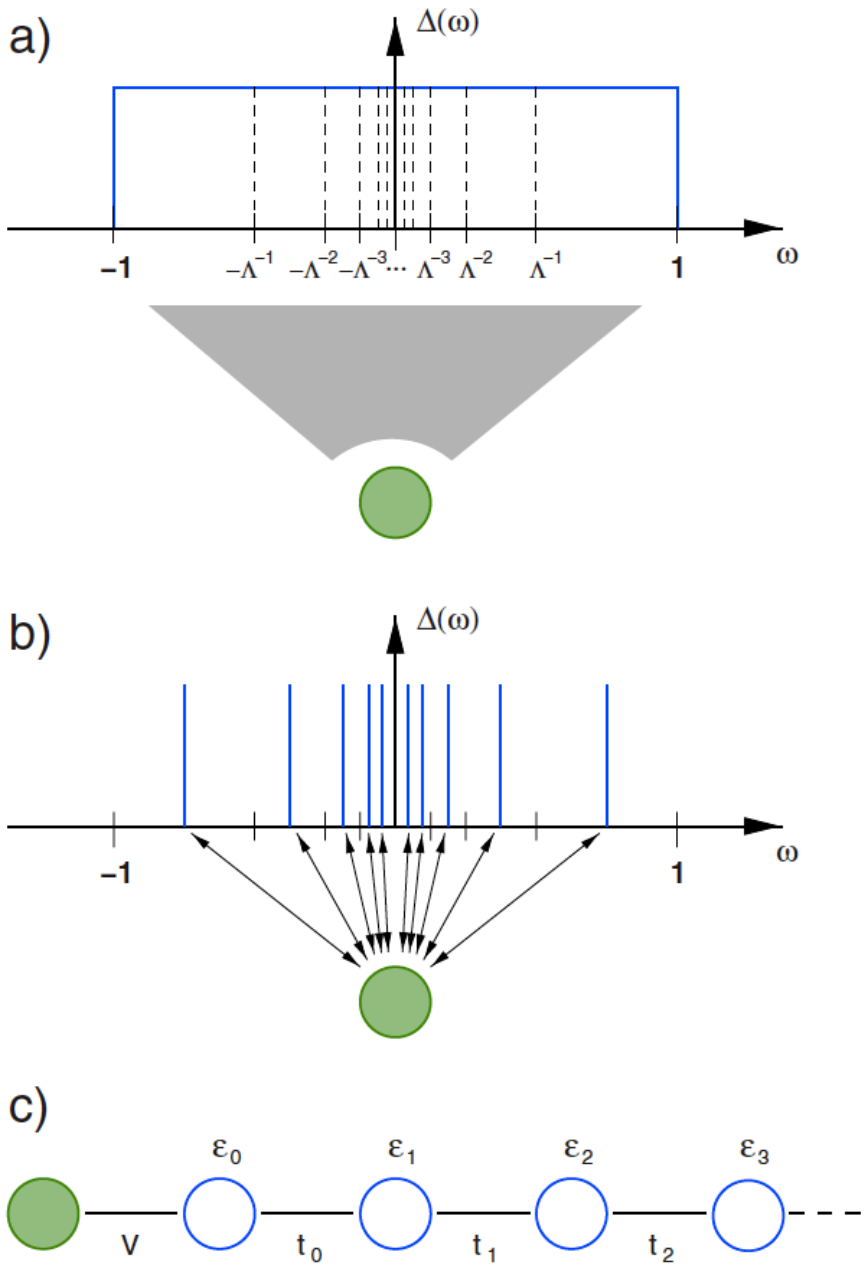

Figure 1.4.1: (Figure source: [9]) Initial steps of the NRG calculation for the SIAM. The impurity (green circle) is coupled to a continuous conduction band. (a) The band is divided into intervals of exponentially decreasing size. (b) The continuous spectrum is replaced by a set of single states. (c) The model is mapped onto a semi-infinite tight-binding Wilson chain.

3. It is now possible to transform the Hamiltonian of the discretized model into the Hamiltonian of a semi-infinite chain of noninteracting electrons with the impurity as its 0th site. For the SIAM, the hopping elements t_n of the chain model fall off as $t_n \propto \Lambda^{-n/2}$. The sites of the chain correspond to a sequence of energy-shells centered around the impurity [9].

4. The key step follows, in which renormalization enters the picture. The outer shell is integrated out, and the resulting model is again stretched to fit the whole bandwidth. Technically, the chain model is solved in an iterative way, starting from the impurity, adding one site of the chain in each step. Successive Hamiltonians are linked by recursion relations, $H_{N+1} = R(H_N)$ (Eq. (36) in Ref. [9]), which is a specific expression of the renormalization group equation[9]. The calculation is finished at a finite length of the chain when a fixed point is reached. This corresponds to the ground state of the system (or close-to-zero temperature).

5. A necessary part of the iterative procedure is another approximation, truncation of the spectrum. In each step, the Hamiltonian H_N is diagonalized, and characterized by its eigenenergies E_N and the corresponding eigenstates $|r\rangle_N$. Next, the $N+1$ chain site is added, and the basis for H_{N+1} is a tensor product of $|r\rangle_N$ and a suitable basis for the new chain site. Consequently, the Hilbert space blows up exponentially. It is therefore necessary to limit the number of eigenenergies kept in each step only to some maximum number of lowest lying eigenstates. The numerical error introduced by choosing a truncation parameter needs to be checked.

The output of a NRG calculation is the flow of eigenenergies E_N, as well as (possibly) the low-temperature values of various thermodynamic and transport properties.

This work uses the NRG implementation called NRG Ljubljana developed by Rok Žitko [74, 75, 77] to solve the superconducting quantum dot setup.[10] Problem initialization is done in Mathematica using the SNEG package [76] for performing calculation with second quantization operators. The iterative diagonalization of the Wilson chain is implemented in C++. The input Hamiltonian and a sample input parameter file can be found in Appendix C.

[9] More accurately, due to parity effects, the renormalization group transformation corresponds to two successive steps of the calculation $H_{N+2} = R^2(H_N)$. The results may differ for even and odd steps in some models [75].

[10] The NRG Ljubljana code has been in continued development, and versions 2.3 and 2.4 have been used.

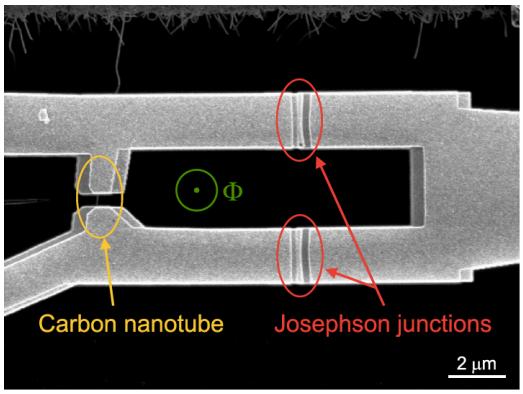

Figure 1.5.1: (Figure source: [4]) Scanning electron microscope image of a carbon nanotube quantum dot embedded in a SQUID loop. The "large" Josephson junctions have a much higher critical current than the "small" carbon-nanotube junction. The setup is phase-biased by the magnetic flux Φ through the loop, and allows for the measurement of both the differential conductance and the current-phase relations of the CNT junction.

1.5 Recent experiments on superconducting carbon nanotube quantum dots

Experiments with superconducting quantum dots have now a history of two decades. Proximity-induced supercurrent through a single-walled carbon nanotube has been measured in 1999, Refs. [33, 48]. The Kondo effect in a sc-QD has been observed in 2002 [7], and a gate-controlled $0 - \pi$ transition has been first measured in a semiconductor nanowire [66], and in carbon nanotubes in [14] and [31] (successfully interpreted via sc-SIAM and QMC in Ref. [40]). Andreev bound states have been observed in e.g. Refs. [54, 10, 58]. More sc-CNT experiments include [51, 73, 24, 43].

While numerous, these experiments remain difficult, and are getting more and more refined in recent years. This thesis contributes to the interpretation of two experiments by Laboratoire de physique des solides, Orsay, which I will briefly introduce in the following subsections: Detailed measurement of the current-phase relations [20, 21, 19], and the measurement of the AC Josephson effect in the Kondo regime of the quantum dot, published in Paper III.

1.5.1 Current-phase relation measurement

The experimental measurement of the current-phase relations in question has been first announced in Ref. [20] and explored in detail in Refs. [21, 19]. It is based on embedding the carbon-nanotube junction into a SQUID device with three junctions, described in Ref. [4] (see also Fig. 1.5.1). The SQUID contains the carbon nanotube junction we are interested in and two reference Josephson junctions with a much higher critical current. Through this cleverly constructed circuit, it is possible to measure both the current-phase relations and the differ-

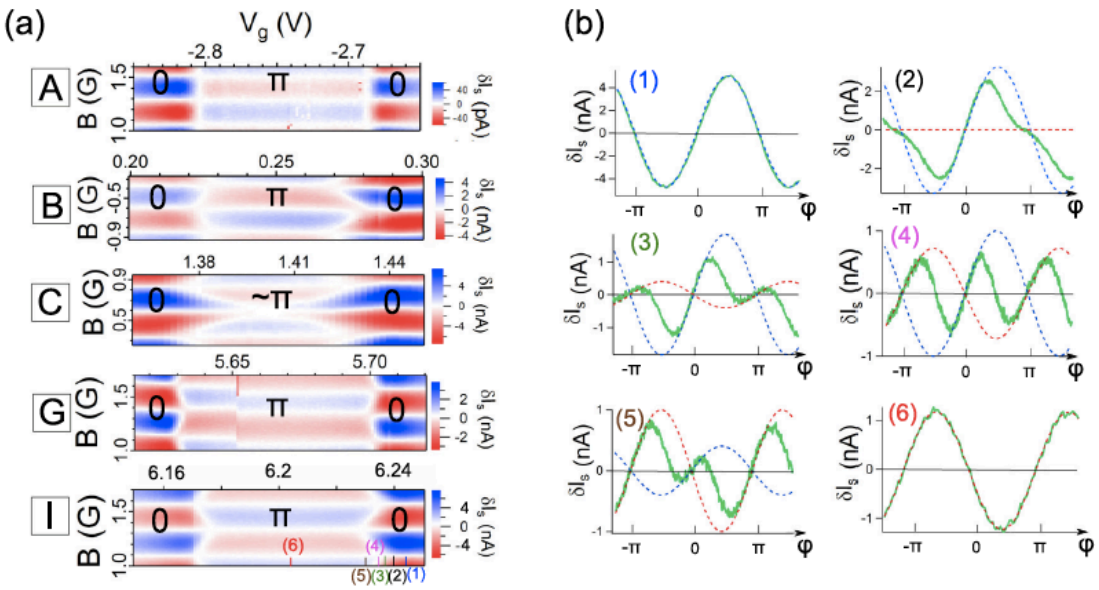

Figure 1.5.2: (Figure source: [21]) Current-phase relations of a superconducting carbon nanotube quantum dot, measured by Delagrange, et al. (a) Switching current as a function of gate voltage and magnetic field, for different Coulomb diagrams which exhibit a $0-\pi$ transition (labeled A,B,C,G,I in Fig. 1.1.2). (b) Current-phase relations for diamond I (green line) near the transition. The dashed lines are guides to the eyes, representing sine dependencies typical for the 0 and π phases.

ential conductance of the carbon nanotube.

In Ref. [21], two CNT samples were measured, and we are mostly interested in one of them. It was made of a carbon nanotube and Pd/Nb/Al leads with a small superconducting gap $\Delta = 0.17$ meV. First, the junction was characterized in a non-superconducting state, achieved by applying a magnetic field (a strong field $B = 1$T was necessary to destroy superconductivity in the Pd/Nb/Al lead). The differential conductance was measured and the observed Coulomb diamonds were used to determine parameters of the CNT quantum dot (please refer back to Fig. 1.1.2 in Sec. 1.1.5, where I've used it to illustrate the broken four-fold degeneracy of a CNT). Coulomb interaction U and total coupling Γ were determined for each gate-voltage region separately. In Ref. [21], for most diamonds except one, the coupling asymmetry $a = \Gamma_L/\Gamma_R$ wasn't determined. I have fitted the coupling asymmetry from the available experimental results as part of my thesis work, and this is the topic of Sec. 2.1.4).

Next, the differential conductance and the switching current in the superconducting state of the junction are measured. In several Coulomb diamonds with occupation number $n = 1$ (see blue squares in Fig. 1.1.2) the $0-\pi$ transition has been observed. Those regions are chosen for more detailed current-phase relation measurement, featured in Fig. 1.5.2.

Fig. 1.5.2a displays the switching current as a function of the magnetic field B in the SQUID (which is proportional to the superconducting phase difference φ) and the gate voltage (which is directly proportional to ε). From this measure-

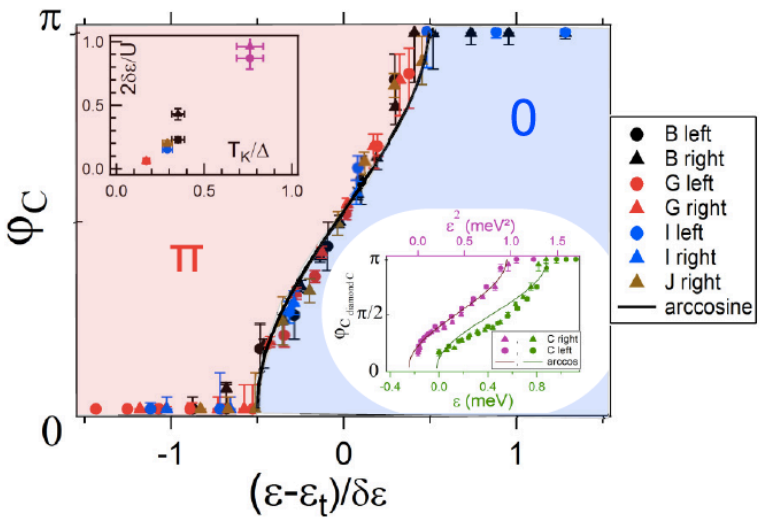

Figure 1.5.3: (Figure source: [21]) The critical phase φ_C dependence on the level energy ε, shifted and rescaled by the width of the transition (see Eq. (1.5.1) in the main text). The measured phase transitions for several Coulomb diamonds fall on an arccosine curve. Inset: Same for Coulomb region labeled C, where the transition doesn't span the whole range of φ and doesn't fit the arccosine.

ment, current-phase relations are extracted. Fig. 1.5.2b shows the current-phase relations in one of the Coulomb diamonds, progressively changing with level energy ε. While sinusoidal CPRs corresponding to the zero phase are observed on one side of the diamond, and CPRs with smaller amplitude and opposite sign corresponding to the π phase can be seen in the middle of it, there is a transition region with a finite width $\delta\varepsilon$ where the junction isn't fully in either phase. In this transition region a mix of both the $0-$ and $\pi-$phase dependencies is identified in the CPRs, and the authors identify a critical point φ_C where the $0-\pi$ transition in the superconducting phase difference φ takes place[11]. The ε dependence of φ_C is studied (see Fig. 1.5.3). The authors conclude, that for several diamonds $\varphi_C(\varepsilon)$ can be mapped on the same arccosine curve given by

$$\varphi_C = \arccos\left\{-2\frac{\varepsilon-\varepsilon_t}{\delta\varepsilon}\right\} \tag{1.5.1}$$

where $\delta\varepsilon$ is the width of the transition region in ε and ε_t is a linear shift.

We will further discuss this dependence in Sec. 2.1.4, where we also use results of this thesis to estimate the coupling asymmetry of this experimental setup.

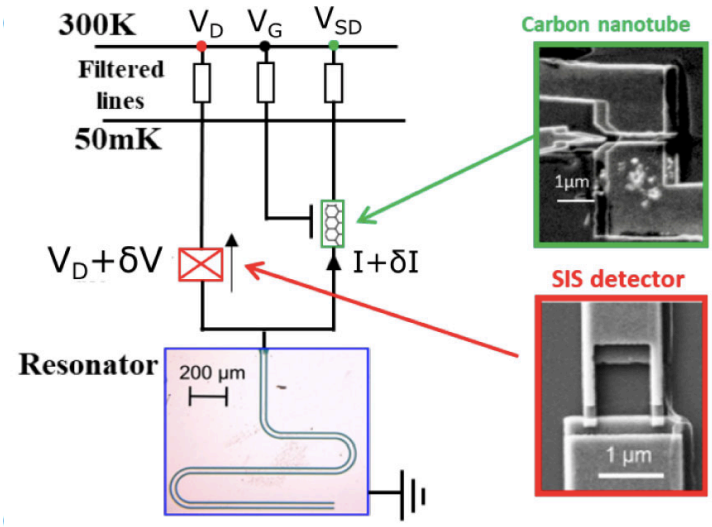

Figure 1.5.4: (Figure source: Paper III) AC Josephson effect measurement scheme. The carbon-nanotube Josephson junction is biased by voltage V_{SD} and emits Josephson radiation, which is absorbed by a simple superconductor-insulator-superconductor Josephson junction detector. The resonator is used to filter out a single frequency line.

1.5.2 High-frequency AC Josephson emission in the Kondo regime

Through the experimental work in Laboratoire de physique des solides, Orsay, it has also become possible to measure the AC Josephson effect in a carbon nanotube quantum dot. Preliminary results on a sample with Pd/Nb/Al contacts have already been published in the thesis of R. Delagrange [19], and more quantitative results on a sample with Pd/Al contacts and $\Delta = 0.05$ meV can be found in the thesis of D. Watfa [69] and in our collaborative Paper III.

The AC Josephson effect measurement is done by detecting the microwave radiation emitted by the CNT Josephson junction (see Fig. 1.5.4). Under voltage bias V_{SD} (source-drain), alternating current with the amplitude I_C^{AC} is induced in the CNT junction, and Josephson radiation with frequency $\nu_J = 2eV_{\mathrm{SD}}/h$ is emitted[12]. This electromagnetic radiation is captured by a second Josephson junction with a known current-voltage characteristics $I_D^0(V_D)$, which acts like a detector in this setup, and photo-assisted (PAT) current I_{PAT} is induced. A superconducting waveguide resonator is constructed to filter out a narrow frequency range around $\nu_0 = 12.5$ GHz, and possibly its odd harmonics. The PAT current induced by Josephson radiation is proportional to the amplitude of the Josephson current

[11] In Ref. [21] the critical point φ_C is estimated as the point where the CPR first crosses zero when going from the region which is closer to sine dependence to the region closer to cosine dependence. This assumption was supported by a quadratic extrapolation of finite temperature Monte-Carlo data to zero temperature. We discuss in detail in Paper II why this is principally wrong - however, the practical difference is not too big and doesn't invalidate the analysis of the $\varphi_C(\varepsilon)$ dependence in Ref. [21].

[12] A near-sinusoidal current-phase relation is assumed (and confirmed through NRG calculations for the DC current, see Sec. 2.2.1) and higher harmonics are neglected.

I_C^{AC} squared

$$I_{\mathrm{PAT}} \simeq \frac{\left(I_C^{\mathrm{AC}}\right)^2}{V_{\mathrm{SD}}^2} I_D^0(V_D + 2V_{\mathrm{SD}})\,, \tag{1.5.2}$$

and the proportionality constant depends on the impedance of the resonant circuit [3]. To match the resonator frequency ν_0, the bias voltage needs to be tuned to $eV_{\mathrm{SD}} = h\nu_0/2 \approx 26\ \mu$V, which is about half of the superconducting gap $\Delta/2$ for the sample in question. This is the energy where the signal from the Josephson radiation is expected. (Supplemental material to Paper III contains details on separating the signal from the background of the measured PAT current, as well as details on sample characterization, sketched below.)

The AC Josephson effect measurement is accompanied by complementary measurements used for sample characterization. First, differential conductance as a function of gate voltage and bias voltage in the non-superconducting regime is measured, where superconductivity is, again, suppressed by the magnetic field. Due to the small size of the superconducting gap, a field of 0.1 T suffices. This allows for the Kondo effect to be clearly visible in the normal state dI/dV. The Kondo temperature of two regions (labeled A and B) is extracted from temperature-dependent conductance, and the parameters U, Γ and coupling asymmetry a are determined from normal-state measurements. Second, the DC Josephson effect is also measured. The critical current is extracted using the RCSJ model [31]. Note that, unlike the experiment described in previous section, there is no control over the superconducting phase difference, so the CPR can't be measured. The DC Josephson current however suggests, that the CNT junction stays in the $0-$phase in the entire range of gate-voltages, a picture that I confirmed with NRG calculations (see Sec. 2.2).

The most surprising result of this work is a drop in the AC Josephson current observed in regions where the Kondo effect is visible in the normal state differential conductance. This kind of behavior is not seen in the DC case. Fig. 1.5.5 features a comparison of both supercurrents: In regions A and B, the amplitude of the AC Josephson current drops significantly in the Kondo region, while the DC Josephson current is at its highest. This is not observed in control region C, which exhibits no Kondo features.

In Paper III we suggest an explanation of this effect based on quasiparticle dynamics. A comparison of the measurement result to the AC Josephson emission expected in the quantum point contact is given in supplemental material to Paper III and in Sec. 2.2 of this thesis.

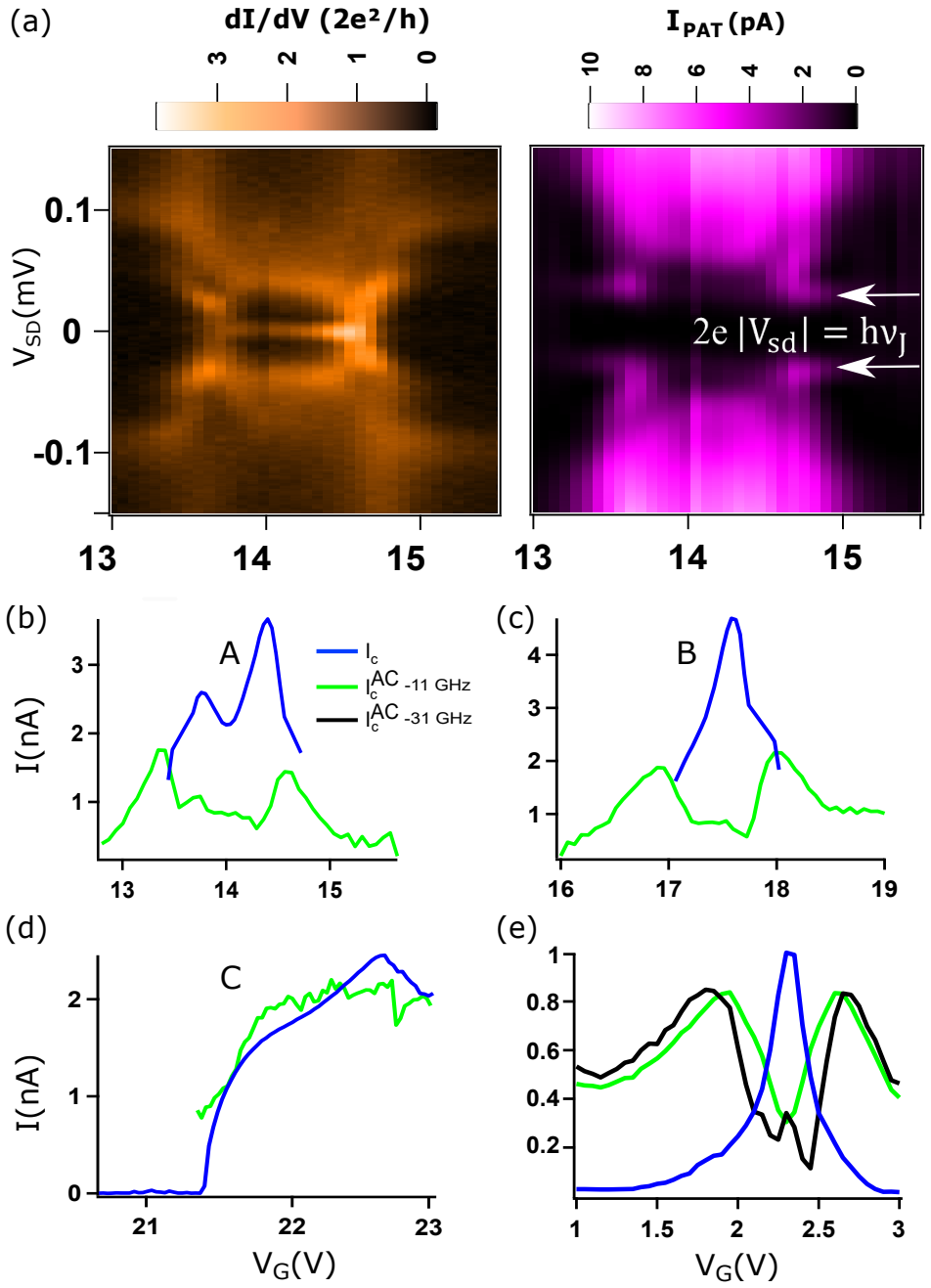

Figure 1.5.5: (Author of figure: Diana Watfa) Differential conductance and photo-assisted current. (a) Differential conductance dI/dV in the superconducting state and PAT current I_{PAT} as a function of bias voltage V_{SD} and gate voltage V_G for Kondo region A. (b)-(d) Critical currents I_C for the DC Josephson effect, and I_C^{AC} for the AC Josephson effect for Kondo regions A, B and control region C. (e) Same for the Pd/Nb/Al sample and two resonator frequencies (the I_C curve has been downscaled 10x).

Chapter 2

Results and discussion

This chapter presents the results of my thesis and their implication for further research. Section 2.1 deals with the DC Josephson effect in a superconducting QD, especially with the $0-\pi$ transition, and summarizes a part of the research published in Papers I and II, most importantly the influence of coupling asymmetry, which has been previously missed in literature. Section 2.2 concerns my contribution to interpreting the measured AC Josephson emission of a superconducting carbon nanotube under constant voltage bias, in the experiment described in Sec. 1.5.2, expanding on the published supplement to Paper III.

2.1 Phase-biased superconducting SIAM with coupling asymmetry

In this section, I consider a phase-biased quantum dot Josephson junction (only the DC Josephson effect being responsible for the supercurrent). Such a setup has been experimentally realized as described in Sec. 1.5.1. I introduce the symmetry-asymmetry relation and its derivation (Secs. 2.1.1 and 2.1.2), discuss the influence of asymmetry in the Kondo regime specifically (Sec. 2.1.3), and apply the symmetry asymmetry relation to experiment (Sec. 2.1.4). In the whole chapter, I keep the condition $\Delta = \Delta_L = \Delta_R$, which is necessary for the validity of the symmetry-asymmetry relation (Sec. (2.1.1)) and results which follow from it.

2.1.1 Symmetry-asymmetry relation

Previously, most theoretical studies about the sc-SIAM (defined by the Hamiltonian (1.3.1)) have focused on the presumably simplest case of symmetric dot-leads coupling, $a = \Gamma_L/\Gamma_R = 1$. The role of asymmetric coupling had not been clarified, and often it had been neglected entirely in the interpretation of experiments, especially in the Kondo regime, where universal dependence on T_K/Δ *only* was assumed. What we call the symmetry-asymmetry relation is a simple analytical relation, derived by using Green's function of the superconducting quantum dot, which links the physics of an asymmetric sc-SIAM model to its effective symmetric equivalent. Let us have a look at the its derivation and consequences.

Inspecting the non-interacting Matsubara Green's function $\widehat{G}_0(i\omega_n)$ (Eq. (1.3.6)), we notice that it only depends on $\varphi_{R,L}$ through its off-diagonal element $\Delta_\varphi(i\omega_n)$, which under the assumption $\Delta_L = \Delta_R$ becomes

$$\Delta_\varphi(i\omega_n) = \frac{\Delta}{\sqrt{\omega_n^2 + \Delta^2}}(\Gamma_L e^{i\varphi_L} + \Gamma_R e^{i\varphi_R}).$$

Importantly, the φ dependence is only contained in the $\Gamma_L e^{i\varphi_L} + \Gamma_R e^{i\varphi_R}$ factor, which is frequency independent. Rewriting this complex number into an amplitude and phase notation, and denoting the average phase of the junction $\delta = \frac{1}{2}(\varphi_L + \varphi_R)$, we get

$$\Gamma_L e^{i\varphi_L} + \Gamma_R e^{i\varphi_R} = \Gamma\sqrt{\chi(\varphi, a)}e^{i(\delta + \Psi(\varphi, a))} \tag{2.1.1}$$

with

$$\chi(\varphi, a) = 1 - \frac{4a}{(a+1)^2}\sin^2\frac{\varphi}{2} \tag{2.1.2}$$

and

$$\Psi(\varphi, a) = \arctan\left[\left(\frac{a-1}{a+1}\right)\tan\frac{\varphi}{2}\right]. \tag{2.1.3}$$

Note the function $\chi(\varphi, a)$ given by Eq. (2.1.2) as it will from now on be used any time we discuss the influence of asymmetry on the sc-SIAM. Function $\chi(\varphi, a)$ and the phaseshift $\Psi(\varphi, a)$ together set both the φ-dependence and the asymmetry dependence$\widehat{G}_0(i\omega_n)$. We can equate the amplitude and phase of (2.1.1) of an asymmetric system to the amplitude and phase of an effective symmetric system with the same Γ. Namely we choose combinations of φ and a so that the value of $\chi(\varphi, a)$ remains constant

$$\chi(\varphi^S, 1) = \chi(\varphi^A, a)\,, \tag{2.1.4}$$

and choose the average phase of the symmetric system so that

$$\delta^S = \delta^A + \Psi(\varphi^A, a)\,. \tag{2.1.5}$$

Superscripts S, A denote the cases of symmetric and asymmetric coupling. The transformation keeps $\widehat{G}_0(i\omega_n)$ unchanged, and expresses therefore an invariant property of the quantum dot system. Moreover, this invariance caries over to the *interacting* case. This is because the *full* Green's function $\widehat{G}(i\omega_n)$ is a functional of $\widehat{G}_0(i\omega_n)$, only further depending on the interaction strength U [41]. The phase-shift δ^S in (2.1.5) is important for this derivation, but usually insignificant in practical calculations due to gauge freedom (this is fully true for on-dot quantities, and discussed in the next section). Therefore only Eq. (2.1.4) needs to be satisfied, and it's Eq. (2.1.4) that we call the *symmetry-asymmetry relation.* Note that in the symmetric case $\chi(\varphi, a)$ reduces to $\chi(\varphi^S, 1) \equiv \cos^2\frac{\varphi^S}{2}$. The value range of $\chi(\varphi^S, 1)$ is $[0, 1]$, and shrinks to $\left[\left(\frac{a-1}{a+1}\right)^2, 1\right]$ for $\chi(\varphi, a)$. Together

with continuity and monotony of function $\chi(\varphi^A, a)$ this implies that a suitable φ^S exists for any $\varphi^A \in (0, 2\pi)$, and Eq. (2.1.4) can be expressed as[1]

$$\varphi^S = 2\arccos\sqrt{\chi} = 2\arccos\sqrt{1 - \frac{4a}{(a+1)^2}\sin^2\frac{\varphi^A}{2}} \tag{2.1.6}$$

It's inversion, where defined, reads

$$\varphi^A = \arccos\left(\frac{(a+1)^2}{2a}(\chi - 1) + 1\right) = \arccos\left(1 - \frac{(a+1)^2}{2a}\sin^2\frac{\varphi^S}{2}\right). \tag{2.1.7}$$

The symmetry-asymmetry relation allows us to describe the physics of any asymmetric junction in terms of the properties of it's symmetric counterpart, a junction with the same total coupling Γ and $a = 1$. The properties of the symmetric junction usually still must be computed numerically, but we get a number of advantages:

- the numerics must only be done once to know the properties of a junction with any asymmetry
- the asymmetry can be estimated from experimental data by fitting
- effectively, we have a system with less independent variables, as φ and a are related through χ.

We now look explicitly at the consequences of the symmetry-asymmetry relation for different kinds of physical quantities. First, the 0-π phase boundary, which (at zero temperature, in a suitable parameter range) happens at a particular critical phase difference φ_C, is only influenced by the relation between φ_C^S and φ_C^A, and Eq. (2.1.6) applies directly.

For physical quantities which only depend on the local Green's function $\widehat{G}$ (such as the Free energy and the induced gap), the symmetry-asymmetry relation becomes a substitution relation

$$F^A(\varphi^A) = F^S(\varphi^S)\ , \tag{2.1.8}$$

where $F^S(\varphi^S)$ is the (known) functional dependence of the quantity in question on φ^S. Explicitly, substituting from (2.1.6)

$$F^A(\varphi^A) = F^S\left(2\arccos\sqrt{1 - \frac{4a}{(a+1)^2}\sin^2\frac{\varphi^A}{2}}\right). \tag{2.1.9}$$

[1]We can also relate two cases with different asymmetry, if needed. In that case the relation (2.1.4) reads $\chi(\varphi_1, a_1) = \chi(\varphi_2, a_2)$, and inserting Eq. (2.1.2) into Eq. (2.1.7), we obtain

$$\varphi_1 = 2\arcsin\left(\frac{\sqrt{a_2}(a_1+1)}{\sqrt{a_1}(a_2+1)}\left|\sin\frac{\varphi_2}{2}\right|\right)$$

The second junction should be less symmetric ($a_2 > a_1$ for $a_{1,2} > 1$) in order for φ_1 to match every φ_2.

To get a graphical idea, this means that the function $F^S(\varphi^S)$ is "cut off" at a certain maximal value of φ^S (which is $\varphi^S = 2\arccos\sqrt{1-\frac{4a}{(a+1)^2}} = 2\arcsin\sqrt{\frac{4a}{(a+1)^2}}$) and "stretched" by the transformation (2.1.7) to fill all the definition range of φ^A, $\varphi^A \in (0, 2\pi)$.

Finally, let's talk about the Josephson current, which is not a local on-dot quantity, and depends explicitly on the leads. To derive the corresponding form of symmetry-asymmetry relation from definition can be tedious (see next section and Appendix A to Paper I. However, the easiest way to compute the Josephson current indirectly is to take the derivative $\mathcal{J} \equiv \frac{2e}{\hbar}\frac{\partial F}{\partial \varphi}$ of the free energy F, which is an on-dot quantity and satisfies (2.1.9). Consequently, a prefactor appears in the symmetry-asymmetry relation for the supercurrent:

$$\begin{aligned}\mathcal{J}^A(\varphi^A) =& \frac{\cos\frac{\varphi^A}{2}}{\sqrt{\frac{(a+1)^2}{4a} - \sin^2\frac{\varphi^A}{2}}} \times \\ & \mathcal{J}^{\mathcal{S}}\left(2\arccos\sqrt{1-\frac{4a}{(a+1)^2}\sin^2\frac{\varphi^A}{2}}\right),\end{aligned} \tag{2.1.10}$$

where again $\mathcal{J}^S(\varphi^S)$ is the φ dependence of the Josephson current in the symmetric case. The prefactor ensures $\mathcal{J}^A(\pi) = 0$.

2.1.2 Gauge invariance of the Josephson current

The concept of gauge invariance in the context of superconductivity implies that physical quantities must only depend on the superconducting phase difference φ (or, in case of continuous change, on the gradient), not the absolute value of the superconducting phase itself (see e.g. Ref. [27] on a pedagogical discussion on electromagnetic gauge invariance in the BCS theory). In the language of the previous paragraph, for a system with two superconducting leads, gauge invariance states that we can add a constant to both $\varphi_{L,R}$, or, we can freely choose $\delta = \frac{1}{2}(\varphi_L + \varphi_R)$. This is, however, true for measurable quantities only - Green's functions may depend on δ explicitly.

In the case of the symmetry-asymmetry relation, we are not talking about *one* system, but *two* systems. As stated previously, to keep the factor (2.1.1) (and thus the local impurity Green's function $\widehat{G}_0$) constant, we should equate both its amplitude and the phase by the already known relations

$$\chi(\varphi^S, 1) = \chi(\varphi^A, a) \tag{2.1.11}$$

and

$$\delta^S = \delta^A + \Psi(\varphi^A, a) \tag{2.1.12}$$

with functions $\chi(\varphi, a)$ and $\Psi(\varphi, a)$ defined by Eqs. (2.1.2) and (2.1.3). Note that the function $\Psi(\varphi^A, a)$ dependents on φ^A and as such cannot be gauged away. In this section I would like to clear up some confusion about the second equation (2.1.12), and when it is needed.

As mentioned in the last chapter, Eq. (2.1.12) is necessary to explain why the symmetry-asymmetry relation is valid for interacting ($U \neq 0$) sc-QD systems. The full interacting Green's function $\widehat{G}(i\omega_n)$ is a functional of $\widehat{G}_0(i\omega_n)$. Suppressing the dependence of $\widehat{G}_0$ on ε and the total Γ we can write $\widehat{G} = \widehat{G}[\widehat{G}_0(\varphi, \delta, a), U]$. Because Green's functions need not be gauge invariant, the dependence of $\widehat{G}$ and $\widehat{G}_0$ on the phase of Δ_φ (the off-diagonal element of $\widehat{G}_0$) may be non-trivial. Eq. (2.1.12) is essential to make the phases of Δ_φ and thus $\widehat{G}_0$ equal for the symmetric and asymmetric systems. The symmetry-asymmetry relation on the level of Green's functions reads

$$\widehat{G}[\widehat{G}_0(\varphi^A, \delta^A, a), U] = \widehat{G}[\widehat{G}_0(\varphi^S, \delta^S, 1), U]\,, \tag{2.1.13}$$

assuming both Eq. (2.1.11) and (2.1.12) implicitly.

When applying the symmetry-asymmetry relation to local physical quantities (those quantities which can be computed from $\widehat{G}$ without depending explicitly on lead properties like φ_α, the density of states in the leads, etc.) the use of Eq. (2.1.12) stays implicit. Taking a local quantity $F[\widehat{G}](\varphi, a)$, the claim of gauge-invariance is, that the measurable $F^{S,A}$ must not depend on $\delta^{S,A}$ in any way. The phaseshifts only enter through Eq. (2.1.13), which leads to $F^A[\widehat{G}](\varphi^A, a) = F^S[\widehat{G}](\varphi^S, 1)$ (which is Eq. (2.1.8)). In all practical calculation, inserting the $\varphi^S(\varphi^A)$ dependence from Eq. (2.1.11) is enough, cf. Eq. (2.1.9).

However, relation (2.1.12) is crucial if we need to make a calculation which depends on φ_α explicitly. Let's take the Josephson current as an example. Expressed as a sum over Matsubara frequencies it reads

$$\mathcal{J}_\alpha = 4k_BT \sum_{\omega_n} \frac{\Gamma_\alpha \Delta}{\sqrt{\Delta^2 + \omega_n^2}} \mathrm{Im}\left[\mathcal{G}(i\omega_n) e^{-i\varphi_\alpha}\right]\,, \tag{2.1.14}$$

where $\mathcal{G}(i\omega_n)$ is the off-diagonal element of the *interacting* Green's function $\widehat{G}(i\omega_n)$. The gauge invariance of $\mathcal{J}_\alpha$ is not obvious from this equation, and I have carried out and published the lengthy calculation in Appendix A to Paper I. In summary, if we want to apply the symmetry-asymmetry relation to the definition of the current (2.1.14) directly, we need to use both Eqs. (2.1.11) and (2.1.12) to first express φ_α^S in terms of φ_α^A.[2] We then apply the equivalence of the real and imaginary part of $\mathcal{G}(i\omega_n)$ for the symmetric and asymmetric systems and, with some effort, recover the gauge-invariant relation (2.1.10) for the Josephson current.

The main take-away from this section is that linking the gauges of the symmetric and asymmetric system by (2.1.12) is necessary, both in the derivation of the symmetry-asymmetry relation, and explicitly in calculating non-local quantities.

2.1.3 Coupling asymmetry and Kondo universality

Our work on asymmetry has also provided an important clarification on the Kondo universality for the $0-\pi$ phase boundary. In the Kondo regime this phase

[2] By adding/subtracting Eq. (2.1.11) in the form $\varphi^S = \varphi_L^S - \varphi_R^S = 2\arccos\sqrt{\chi(\varphi^A, a)}$ and Eq. (2.1.12) in the form $2\delta^S = \varphi_L^S + \varphi_R^S = \varphi_L^A + \varphi_R^A + 2\Psi(\varphi^A, a)$ we obtain $\varphi_{L,R}^S = \frac{1}{2}(\varphi_L^A + \varphi_R^A) + \Psi(\varphi^A, a) \pm \arccos\sqrt{\chi(\varphi^A, a)}$.

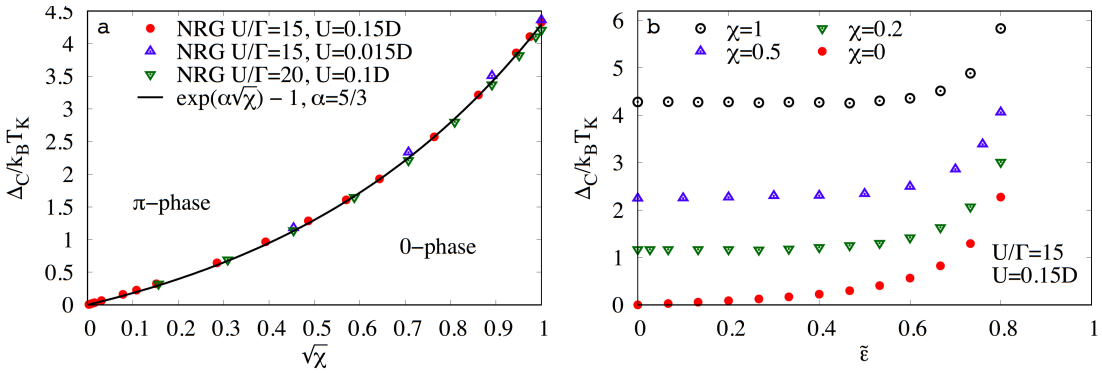

Figure 2.1.1: (a) Universal shape of the ratio of the critical value of the gap Δ_C over the Kondo temperature T_K (2.1.16) as a function of variable χ (2.1.2), in the Kondo regime. The points represent NRG data with $U/\Gamma = 15$, 20 and different values of the bandwidth D. The solid line corresponds to $\Delta_C/k_BT_K = \exp(\alpha\sqrt{\chi})-1$ with $\alpha = 5/3$, see Eq. (2.1.15). (b) The $\tilde{\varepsilon} = (2\varepsilon+U)/U$ dependence of Δ_C/T_K for χ=0, 0.2, 0.5, and 1.

boundary was widely believed to be a universal function of T_K/Δ and specifically to occur at $T_K \approx \Delta$. The symmetry-asymmetry relation implies that even in the Kondo regime coupling asymmetry must play an important role. Nevertheless, we have shown numerically that the phase boundary can indeed be described by a universal function of T_K/Δ if $\chi = \chi(\varphi, a)$ given by Eq. (2.1.2) is used as a variable. The results are summarized here following Paper II.

NRG data is shown in Fig. 2.1.1. Fig. 2.1.1a is a plot of the Δ_C/T_K dependence on $\sqrt{\chi}$, where Δ_C denotes the critical gap - the point for which the phase transition occurs at zero temperature. Zero-temperature data are computed for two different U/Γ values and thus for very different values of T_K (both data sets strongly in the Kondo regime) at half-filling ($\varepsilon = -U/2$). The NRG bandwidth D is also changed to check the accuracy of the calculation - since NRG is based on the wide band approximation, choosing a finite bandwidth influences the data slightly. The figure shows that deep in the Kondo regime the position of the phase-transition boundary can be approximated by the function

$$\frac{\Delta_C}{k_BT_K} = \exp\left(\alpha\sqrt{\chi}\right) - 1\,. \tag{2.1.15}$$

The coefficient α has been fitted to $\alpha = 1.65 \pm 0.02 \approx 5/3$ (differing very slightly for the different data sets). The Kondo temperature is given by

$$k_BT_K \equiv 0.29\sqrt{\Gamma U}\exp\left(-\frac{\pi|\varepsilon|(\varepsilon+U)}{2\Gamma U}\right)\,. \tag{2.1.16}$$

Note the numerical prefactor: For other definitions of T_K, Eq. (2.1.15) and Fig. 2.1.1a must be adequately rescaled. For $\chi = 1$ (corresponding to $\varphi = 0$, which is also the case of a quantum impurity coupled to one superconductor only) the phase transition appears at $\Delta_C/k_BT_K \approx 4.29$, indeed a value of order (but not equal to) one[3].

[3]For another common definition of the Kondo temperature $\tilde{T}_K$ (cf. Eq. (1.1.12)) such that

Fig. 2.1.1b is showing the Δ/k_BT_K dependence on gate voltage, with the level energy ε shifted and normalized to

$$\tilde{\varepsilon} \equiv \frac{\varepsilon + U/2}{U/2} \tag{2.1.17}$$

so that $\tilde{\varepsilon} = 0$ is half-filling. For nonzero values of χ, up to $\tilde{\varepsilon} \approx 0.4 - 0.6$ the phase boundary Δ_C/k_BT_K pretty much adheres to the value predicted by (2.1.15) and plotted in Fig. 2.1.1a[4]. (Note that $\chi = 0$ is only achieved for the very specific case $\varphi = \pi$ and $a = 1$.) This shows the validity of the exponential formula (2.1.15) for a wide range of gate-voltages out of half-filling.

In Eq. (2.1.15) and Fig. 2.1.1a, χ is used as an independent variable, while Δ_C is the dependent one, which is why we chose to use the subscript C in Δ_C (instead of χ_C) to mark that we are talking about an equation for the phase boundary. However, the typical experimental situation stands the other way around: There is a junction with the (known and fixed) gap size Δ and a (possibly also known) coupling asymmetry a. The question then is, if the junction is in the $0-$phase, $\pi-$phase, or if we are going to see the phase transition for a particular phase-difference φ_C. Let's answer the question in detail here:

- If $\frac{\Delta}{k_BT_K} \gtrsim 4.29$, the junction is in the $\pi-$phase for the whole range of $\varphi \in (0,\, 2\pi)$.
- For $\frac{\Delta}{k_BT_K} \lesssim 4.29$, the position of the phase transition is dependent on asymmetry, because the value range of χ, $\chi(\varphi, a) \in \left[\left(\frac{a-1}{a+1}\right)^2, 1\right]$, is asymmetry-dependent. For a symmetric junction ($a = 1$) in half-filling, the $0 - \pi$ transition is always present - the $\pi-$phase being around $\varphi = \pi$. For bigger asymmetries, the left part of the graph 2.1.1a is cut off.
- For small enough Δ/k_BT_K and big enough asymmetry, the junction may stay in the $0-$phase for all values of $\varphi \in (0, 2\pi)$. This happens if χ_C is not in the value range of $\chi(\varphi, a)$ for a given asymmetry, $\chi_C < \left(\frac{a-1}{a+1}\right)^2$.
- Inverting Eq. (2.1.15) gives the position of the phase transition for the junction with a given Δ, $\chi_C = \chi(\varphi_C, a) = \ln\left[\frac{\Delta}{k_BT_K} + 1\right]$. The critical superconducting phase difference φ_C is given from χ_C by Eq. (2.1.7).
- To see what phase is expected for a given junction, one may also evaluate Eq. (2.1.15) in $\chi = \chi(\varphi = \pi, a) = \left(\frac{a-1}{a+1}\right)^2$. If the resulting value of $\Delta_C(\varphi = \pi, a, T_K) > \Delta$, the junction is in the $0-$phase. If on the contrary $\Delta_C(\varphi = \pi, a, T_K) < \Delta$, the junction is in the $\pi-$phase for $\varphi = \pi$.

In conclusion, Fig. 2.1.1a is a significant contribution to the notion of Kondo universality in the sc-QD transport setup. Even in the strong Kondo limit, coupling asymmetry is crucial, changing the position of the phase boundary and even

$0.29\sqrt{2}\, k_B\tilde{T}_K = k_BT_K$ the phase transition occurs at $\Delta_C/k_B\tilde{T}_K \approx 1.76$ for $\varphi = 0$.

[4]Results in Fig. 2.1.1b are in agreement with Ref. [72, Fig. 9a]. Authors of this previous study have tested the ε-independence for two different values of U/Γ and concluded that the universality breaks down in the valence fluctuation regime $|\varepsilon| \lesssim \pi\Gamma$ ($|\tilde{\varepsilon}| \gtrsim 1 - 2\pi\Gamma/U \approx 0.58$).

influencing if there is one to begin with. However, universality holds for the phase boundary if coupling asymmetry is included through the χ variable. In addition, the position of the phase boundary can be described by the simple exponential formula (2.1.15).

2.1.4 Symmetry-asymmetry relation applied to experiment

The symmetry-asymmetry relation has been applied to find the asymmetry of the experiment of Delagrange et al. [20, 21, 19], which has been described in Sec. 1.5.1. In the experiment, current-phase relations have been measured, the critical phase φ_C (the point of the phase-transition in φ) has been determined, and the dependence of φ_C on ε has been studied. In the original analysis, the Coulomb interaction strength U and the total Γ are known from experiment, but the coupling asymmetry is not.

For several measured regions, the authors of Ref. [21] fitted the $\varphi_C(\varepsilon)$ by an arccosine curve with a linear dependence on ε,

$$\varphi_C = \arccos\left\{-2\frac{\varepsilon-\varepsilon_t}{\delta\varepsilon}\right\} \tag{2.1.18}$$

where $\delta\varepsilon$ is the width of the transition region in ε and ε_t is a linear shift. After introducing the symmetry-asymmetry relation, the arccosine dependence can now be understood by referring to Eq. (2.1.7), where φ_C is expressed in terms of χ_C. This equation shows clearly that $\varphi_C(\epsilon)$ has an exactly arccosine shape if and only if $\chi_C(\epsilon)$ is linear in ϵ.

To explore the range of validity of this experimental finding, we compute the phase boundary for different values of U, see Fig. 2.1.2. Fig. 2.1.2a is a phase diagram in the $\varphi-\varepsilon$ plane, while the curves $\chi_C(\epsilon)$ are visualized in Fig. 2.1.2b. We observe that, while for small U there is a quadratic $\chi_C(\varepsilon)$ dependence, approaching the Kondo regime with increasing U the boundary becomes linear. Moreover, when asymmetry is involved, only the values of χ close to 1 are used. This means that for large asymmetry a linear approximation becomes relevant for a wide range of parameters.

With this in mind, we approximate $\chi_C(\varepsilon)$ by $\chi_{\mathrm{C}}(\varepsilon) \approx 1-(\varepsilon-\varepsilon_1)/\beta$, where $\chi_C(\varepsilon_1) = 1$ and β is minus the slope of the $\varepsilon(\chi_C)$ dependence. Inserting the expansion into Eq. (2.1.7) we obtain

$$\varphi_{\mathrm{C}}^{A} = \arccos\left(-\frac{(a+1)^2}{2a}\frac{1}{\beta}(\varepsilon-\varepsilon_1)+1\right). \tag{2.1.19}$$

Comparison of Eqs. (2.1.18) and (2.1.19) leads to

$$\delta\epsilon = \frac{4a}{(a+1)^2}\beta(U,\Gamma,\Delta), \tag{2.1.20}$$

where we have explicitly stated the dependence of β on model parameters. As seen from this last equation, the transition width is proportional to β by a factor

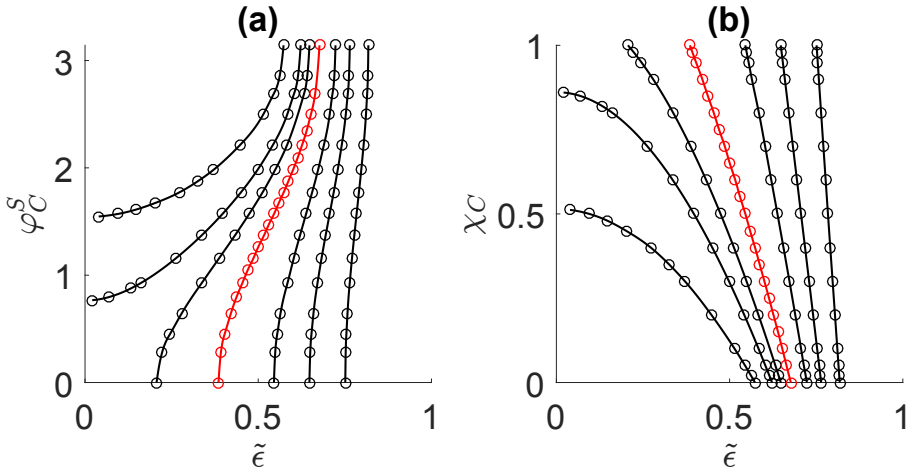

Figure 2.1.2: $0-\pi$ phase diagram. (a) Dependence of the critical phase φ_C on the shifted and normalized level energy $\tilde{\varepsilon} = (\varepsilon + \frac{U}{2})/\frac{U}{2}$, for $\Delta = 0.17$meV, $\Gamma = 0.44$meV, $a = 1$ and different values of U (from left to right the curves belong to $U = \{2, 2.5, 2.8, 3.2, 4, 5, 7\}$ meV). The lines are guide to the eyes. The red line ($U = 3.2$ eV) corresponds to the experimental values of Delagrange et al. [21]. (b) Same as (a) with χ_C on the y-axis. We observe that for increasing U the $\chi_C(\varepsilon)$ dependence becomes more and more linear.

dependent on the asymmetry of the junction (which reduces to 1 for the symmetric case).

In their experiment, Delagrange et al. [21] fitted the $0-\pi$ transitions on both sides of three Coulomb diamonds (called B, G and I in Fig. 1.5.2) with the curve (2.1.18), and determined the transition widths on both sides of the diamond[5]. For diamond I (left side) the asymmetry a=4 was found via Quantum Monte Carlo simulations [20], for B and G it is unknown. The experimental parameters are summarized in table 2.1. I have computed via NRG the $\chi_C(\varepsilon)$ dependence for the parameters U, Γ, Δ given from experiment, and applied Eq. (2.1.20) to find the asymmetry of each diamond, and I will now shortly describe the fitting procedure. Fig. (2.1.3) shows $\tilde{\varepsilon}(\chi_C)$ data computed for diamond B, left side (which is the one with the lowest U/Γ ratio, and consequently also the one which is the *least* linear of the three). As seen in the figure, the slope of the fit for the whole $[0, 1]$ range of χ_C, labeled β^S_{NRG}, differs somewhat from the slope β^A_{NRG} fitted only in the range appropriate for the final asymmetry a_{lin}, $\chi_C \in \left[\left(\frac{a_{lin}-1}{a_{lin}+1}\right)^2, 1\right]$. The fitting range and the asymmetry need to be determined in a (short) self-consistent loop (where β^S_{NRG} is first used to compute an asymmetry via Eq. (2.1.20), this is used compute the range and fit a new slope, which is then used to compute the asymmetry...). The values of β^A_{NRG} and, most importantly, a_{lin}, are again given in table 2.1. The standard fitting error of β^A_{NRG} is bellow 2%, and mostly caused by the imperfect linear approximation (this is, however, negligible compared to the uncertainty of the input parameters). In Paper I we have (on demand of a referee,

[5]Other diamonds (labeled A, C in Fig. 1.5.2) with a single level $0-\pi$ transition were measured, but their transition widths weren't determined.

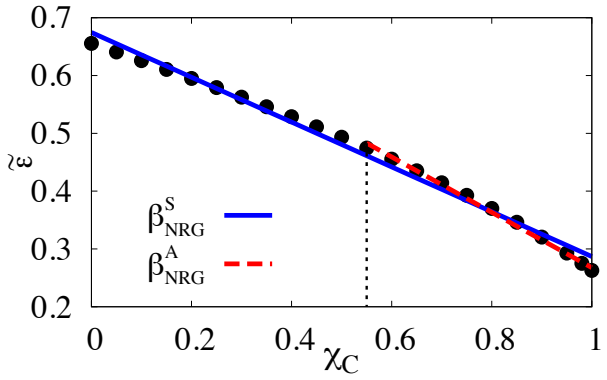

Figure 2.1.3: Obtaining the coupling asymmetry. The numerically determined $\epsilon(\chi)$ dependence (bullets) is approximated by a linear fit in the symmetric (blue line) and asymmetric (red line) case. The negative slopes are denoted β^S_{NRG} and β^A_{NRG} respectively. The fitting range for the asymmetric case is marked by the dashed line, and must be determined self-consistently together with a_{lin}. The data in this figure is computed for Coulomb diamond B, left side, cf. Figs. 1.5.2 and 1.5.3.

	B		G		I	
	left	right	left	right	left	right
U	2.8		3.4		3.2	
Γ	0.43		0.4*		0.44	
Δ	0.17		0.17		0.17	
$\widetilde{\delta\epsilon}_{\rm exp}$	0.23	0.43	0.06	0.06	0.15	0.20
$\beta^A_{\rm NRG}$	0.479	#	0.202	0.202	0.347	0.317
$a_{\rm lin}$	5.8	$1^{\#}$	11	11	6.4	4.0

Table 2.1: Transition width and asymmetry — summary of experimental data [21] and our corresponding results. Columns correspond to the measured Coulomb diamonds. The parameters U, Γ, Δ, given in meV, are known with a 10% (or 20%, marked by *) experimental uncertainty and used as input for NRG calculation. The inverse negative slope β^A_{NRG} (illustrated in Fig. 2.1.3) and the measured transition widths $\widetilde{\delta\epsilon}_{\rm exp} \equiv 2\delta\epsilon_{\rm exp}/U$ are used to determine the asymmetry a_{lin} as discussed in the main text. (#) Here, $\widetilde{\delta\epsilon}_{\rm exp}$ is bigger then the transition width computed from NRG for the case of a symmetric junction, but the difference is within experimental uncertainty.

and considering the success of the GAL approximation in [78]) also considered a quadratic $\chi_C(\varepsilon)$ dependence. The results for the asymmetry are however similar.

Analysis of the right side of diamond I (red lines in Figs. 2.1.2) with the measured transition width $\widetilde{\delta\epsilon}_{\mathrm{exp}} = 0.20$ leads to the asymmetry $a = 4$, which agrees with the value obtained via QMC in Ref. [20]. Even bigger asymmetries were obtained for diamond G and the left sides of diamonds I and B. On the other hand, the large normalized transition width $\widetilde{\delta\epsilon}_{\mathrm{exp}} = 0.43$ measured on the right side of diamond B suggests a symmetric junction. The measured value is actually even wider than the width calculated for the symmetric coupling ($\widetilde{\delta\epsilon} = 0.39$), but the difference is within 10% experimental uncertainty [Paper I].

To conclude, the symmetry asymmetry relation has been successfully used to determine the coupling asymmetry of an experimental setup, where it was previously unknown. The results point towards large asymmetries, and the accuracy of the analysis is limited mostly by experimental uncertainty. The results stress the significance of coupling asymmetry for our understanding of experimental data.

2.2 Interpreting the AC Josephson emission of a carbon-nanotube quantum dot

This section describes my contribution to the characterization of the experiment presented in Sec. 1.5.4 and Paper III. Most of the text in this section has been already made public in supplemental material to Paper III. While I have clarified the underlying ideas with my supervisor T. Novotný and with R. Deblock and D. Watfa, I have written this part of the supplement myself. In this thesis, I have added details especially in Secs. 2.2.3 and 2.2.2.

First, I present the NRG calculation of the DC Josephson effect used to characterize the quantum dot. Second, I give two attempts on explaining the dip which was observed in the AC Josephson current in the Kondo regime of the dot (see Fig. 1.5.5). Due to the combination of out-of equilibrium aspects of the AC Josephson effect and strong Coulomb interaction, it is difficult to describe the AC Josephson effect in the superconducting quantum dot, and has been only attempted in certain regimes [22, 29, 36]. Therefore I wasn't able to perform exact numerical calculations, and instead discuss the similarities and differences between the quantum dot and the quantum point contact, for which the full theory of the AC Josephson effect is available [2, 15].

2.2.1 DC Josephson effect - NRG results

Numerical renormalization group (NRG) calculations, as described in Sec. 1.4, have been performed to understand the DC behavior of the CNT QD. Using the parameters determined from experiment in the non-superconducting state for regions A and B (see table 2.2), the $\varphi-$ and $\varepsilon-$dependent spectra of many-body states and the current-phase relations have been calculated. Fig. 2.2.1a is showing an example of the calculated spectrum of excited sub-gap many-body states (at half-filling, $\varepsilon = 0$), with the ground-state energy equated to zero. The ground state is always a singlet, confirming both regions A and B stay in the 0-phase in the entire range of φ. As described in Sec. 1.3.2, the first excited state is the spin doublet, and its energy difference from the ground state corresponds to Andreev bound state energy E_A. The second excited state is again a singlet, which is not linked to the ground state by single-particle processes, hence it doesn't produce a pair of ABS.

Fig. 2.2.1b shows the current phase relations (corresponding to Fig. 2.2.1a), which are slightly non-sinusoidal, with the critical current in the nanoampere range. The φ dependence of the ABS energy is plotted for multiple values of level-energy ε in Fig. 2.2.1c.

The ε dependent spectra for $\varphi = 0$ and $\varphi = \pi$ are shown in Fig. 2.2.3a-b. With increasing distance from the center of the Coulomb diamond the energy of the excited states increases.

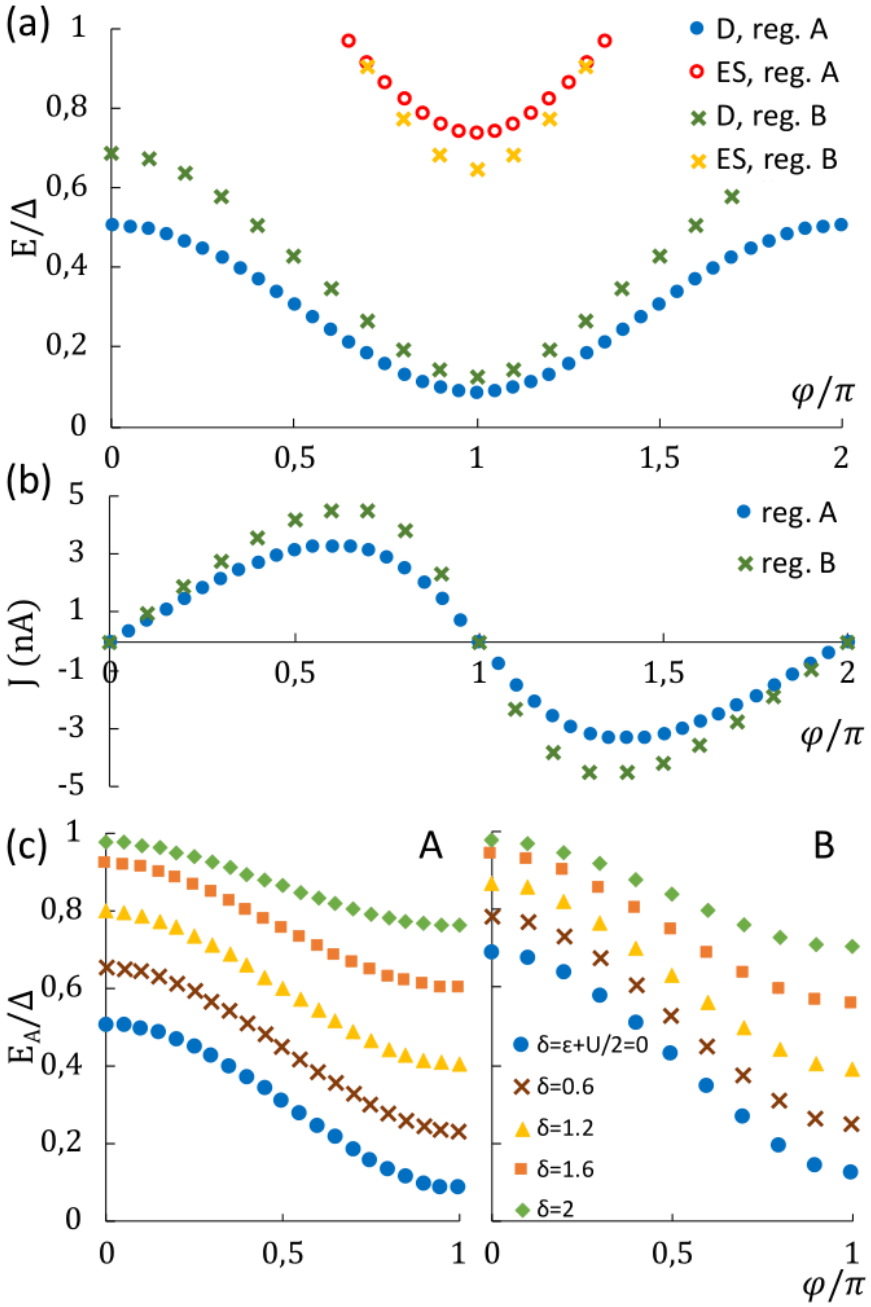

Figure 2.2.1: NRG results (for parameters see Table 2.2). (a) The many-body spectra for Kondo regions A and B and $\varepsilon = 0$. The ground state is a singlet and its energy is set to zero in the NRG. The first excited state is a spin doublet (marked D in the legend) and the second excited state is a singlet (marked ES). This spectrum corresponds to a junction in the 0-phase with one pair of Andreev bound states. (b) The corresponding DC current-phase relations, (c) Andreev bound state energy for chosen values of the level energy ε for regions A and B.

	$T_K(K)$	U (meV)	Γ(meV)	a	Δ(meV)
Kondo A	1.1	3.9	0.62	3.3	0.05
Kondo B	1.7	4	0.75	2.5	0.05

Table 2.2: Parameters of the carbon nanotube quantum dot in Kondo regions A and B determined from the experiment and used as an input to the NRG (see Paper III).

2.2.2 Comparison of the quantum dot and quantum point contact spectra

Quantum dots in the Kondo regime have been sometimes treated like a quantum point contact [71, 67]. The idea is that Coulomb interaction U causes a renormalization of parameters (ABS energies, transmission), but doesn't produce qualitative differences. As long as the junction remains in the zero phase in the entire range of the superconducting phase difference $\varphi \in (0, 2\pi)$, the structure of many-body levels is indeed similar, in both cases consisting of a singlet ground state, an excited spin doublet and an excited spin singlet. There are however important differences.

For a QPC the ABS energy (the difference in energy between the doublet excited state and the ground state) is

$$E_A^{\mathrm{QPC}} = \Delta\sqrt{1 - D\sin^2(\varphi/2)} \tag{2.2.1}$$

(with D the transmission of the junction in the normal state), and the difference between the energy of the excited singlet and the singlet ground state is $2E_A$. With interaction, none of this is true any longer: the ABS don't touch the continuum at $\varphi = 0$, the energy of ABS at $\varphi = \pi$ no longer corresponds to the normal state transmission through Eq. (2.2.1), and the energy difference between the excited singlet and the ground state is significantly higher than $2E_A$. A comparison of the ($\varphi-$dependent) many body spectrum of a quantum point contact vs. NRG data for the interacting quantum dot is shown in Fig. 2.2.2. We choose to equate the ABS energies of the QD and the QPC at $\varphi = \pi$.

In the following subsections, we give two quantum-channel-based interpretations of the experimentally observed drop in the AC Josephson current that seem plausible until a closer look.

2.2.3 Landau-Zener tunneling

In a quantum point contact the variation of $I_C^{AC}(V_{\mathrm{SD}})$ at low bias voltage has been attributed to Landau-Zener (LZ) tunneling [2], a basic quantum mechanical phenomenon occurring at avoided crossings. The probability for this transition to occur is given by [2]

$$P_{\mathrm{LZ}} = \exp\left[-\pi\frac{(\delta E/2\Delta)^2\Delta}{eV_{\mathrm{SD}}}\right]. \tag{2.2.2}$$

We denote δE the energy difference between the states involved in LZ tunneling. For the quantum point contact $\delta E = 2E_A(\varphi = \pi)$, and the quantity $(\delta E/2\Delta)^2 =$

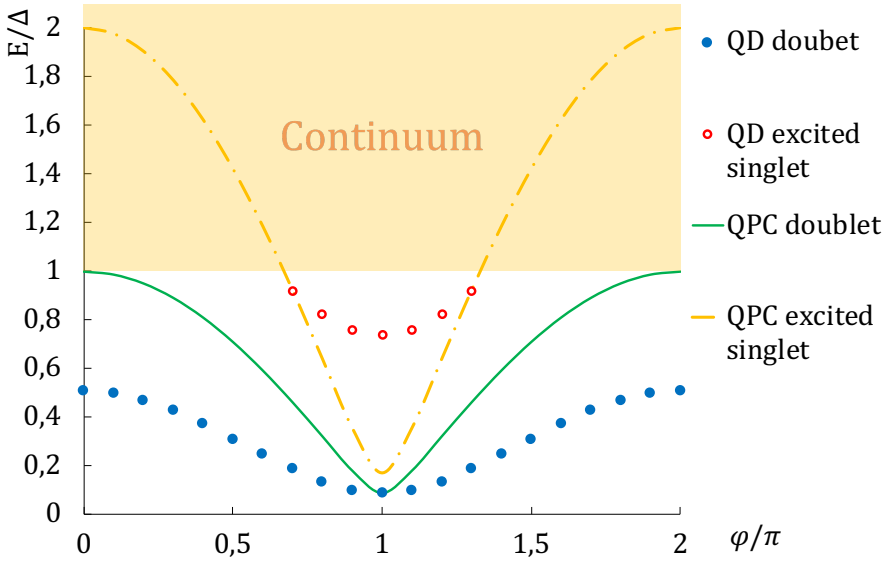

Figure 2.2.2: Comparison of the many body spectrum for Kondo ridge A at the particle-hole symmetry point and the spectrum of a quantum point contact with the same energy of the Andreev bound state at π, as a function of the phase difference φ. The dots represent NRG data for the energy difference between the spin doublet and the ground state corresponding to the ABS energy (blue) and the difference between the excited singlet and the ground state (red). The lines (green, yellow) represent the same quantities for the quantum point contact.

$R = 1 - D$ is the reflectivity of the junction. V_{SD} is the applied voltage, which determines the phase evolution through the Josephson relation $d\varphi/dt = 2eV_{\mathrm{SD}}/\hbar$, and in the experiment $eV_{\mathrm{SD}} \cong \Delta/2$.

Let us insert the ABS energies of the quantum dot into the Landau-Zener probability (2.2.2). With the $\varepsilon-$dependence of $E_A(\varphi = \pi)$ pictured in Fig. 2.2.3b (the doublet, blue), the Landau-Zener probability is close to one at half-filling and drops to zero far away from it, see Fig. 2.2.3d.

Moreover, although the ABS detach from continuum at $\varphi = 0$, the emptying of ABS states at $\varphi = 0$ still happens through Demkov-Osherov tunneling processes. The probability P_{DO} of tunneling between ABS and the continuum, based on Ref. [30], is pictured on Fig. 2.2.3c. Recent work, Ref. [36], has investigated a quantum dot junction with ABS detached from continuum (but still keeping assumptions similar to $\delta E = 2E_A(\varphi = \pi)$) and found that the ratio between P_{DO} and P_{LZ} is significant for the occupation of the states in the junction. In our case $P_{\mathrm{DO}} < P_{\mathrm{LZ}}$ up to $\varepsilon \cong 1.1$ meV, which is where the biggest changes in the experimentally measured current occur. These observations make it very compelling to call Landau-Zener responsible for the measured drop in I_C^{AC}.

However, although LZ tunneling is often pictured as particles tunneling from one ABS to another, on the many body level, it must be a transition from the ground state to the excited singlet state. The jump between the ground state and the spin doublet is forbidden by parity - the singlet and doublet states don't interact at all (this is illustrated by the fact that they can cross in the QD). If there is an avoided crossing, it is between the two singlet states. This means for

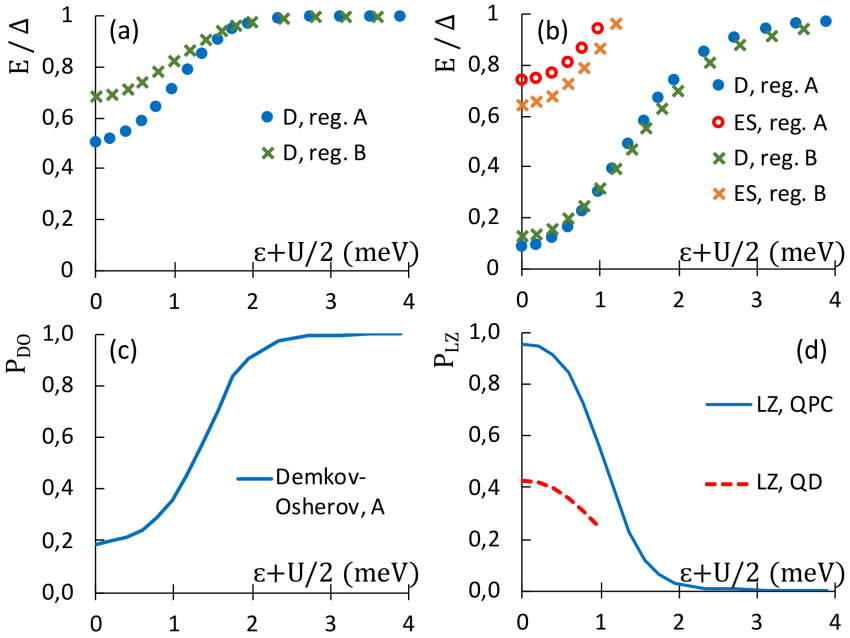

Figure 2.2.3: (a) NRG calculation of the many-body spectrum (ABS energy) at $\varphi = 0$ as a function of the energy level of the QD ε for the Kondo region A. This measures the detachment of the ABS from the continuum of excitation. (b) Same quantity at $\varphi = \pi$. (c) Probability for a QP present in the quantum dot to escape after tunneling into the continuum due to Demkov-Osherov tunneling, region A. This curve is calculated at a voltage $eV{=}\Delta/2$ and use the result derived in Ref. [30]. (d) Calculated Landau-Zener probability, region A. Blue: Using $\delta E = 2E_A$ (see formula (2.2.2)), as for a QPC. Red: Using instead the energy of the excited singlet of the QD.

the quantum dot that instead of taking $\delta E = 2E_A(\varphi = \pi)$ one should consider δE to be the energy of the excited singlet.[6]

For our quantum dot junction the energy of the excited singlet is $\delta E(\varphi = \pi) = 0.74\Delta$ for Kondo region A at half-filling, leading to a transition probability $P_{\mathrm{LZ}}^{\mathrm{QD}} = 0.43$. This value only changes slowly when one goes away from the particle-hole symmetry point (Fig. 2.2.3d). Hence at $\epsilon = 1$ meV, where we see in the experiment that the dynamical supercurrent increases, this Landau-Zener probability is still 0.24 - which makes Landau-Zener tunneling in and of itself unsuitable to explain the observed data.

[6]This is also the case for the QPC - while $\delta E = 2E_A(\varphi = \pi)$ is usually understood as the distance between the two ABS inside the gap, it is nothing other than the energy of the excited singlet. This is a coincidence for the QPC.

While this observation is trivial, none of the people working on this problem noticed for quite a while. This is partly because comprehensive pictures of many-body spectra like Fig. 2.2.2 are not readily available to the community. The quantum point contact is always done in a single-particle picture, only talking about ABS energies, which makes equating ABS energies tempting.

2.2.4 Renormalized QPC based interpretation

The Landau-Zener approach from the previous subsection assumes small bias voltage, which ensures adiabatic development of the system. The interpretation presented now drops this assumption (hardly obvious for $eV = \Delta/2$), and compares the experimental data to the full transport theory for a quantum point contact, which was published in the nineties by Averin and Bardas [2] and Cuevas, Martín-Rodero and Levy Yeyati [15]. These studies feature results for the real and imaginary part of the first Fourier component I_1 of the AC current for several values of transmission. We use their results (read off graphically from their figures) for applied bias voltage $V = \Delta/2e$ to construct the $|I_1(D)|$ dependence of the AC current on transmission, see Fig. 2.2.4a.

Again, we choose to equate the energy of ABS of the QD and the QPC at $\varphi = \pi$. Equating the models means renormalizing the normal state transmission of the quantum dot junction so that it corresponds to $E_A(\varphi = \pi)$ through Eq. (2.2.1), $D = 1 - (E_A(\varphi = \pi)/\Delta)^2$. This renormalized transmission (based on the equilibrium values of $E_A(\epsilon, \varphi = \pi)$ which have been presented in Fig. 2.2.3b) is plotted in Fig. 2.2.4b. Figs. 2.2.4a and 2.2.4b also contain approximative functions[7], which, put together, give us an $|I_1(\varepsilon)|$ prediction. Results for both Kondo ridges A and B are similar and given in Fig. 2.2.4c, quite surprisingly showing a nice semi-quantitative agreement between the renormalized-quantum-point-contact-based prediction and measured experimental data.

Fig. 2.2.4c shows that the drop in the AC current at this particular bias voltage is already expected in a QPC, suggesting similarity. However, this analysis still does not take into account the differences in the many-body spectrum of the quantum point contact vs. quantum dot (illustrated in equilibrium by the detachment of ABS from the continuum and the raised energy of the excited singlet), which raises doubt about its accuracy. Therefore, in Paper III we have decided in favor of a different physical mechanism (the interaction with quasiparticles) to explain the observed voltage drop.

[7]The approximations don't have a physical meaning. The $|I_1(D)|$ dependence at $V = \Delta/2e$ is fitted by $\alpha D^\beta \exp(-\gamma D^\delta) + \kappa D$, and the $D(\epsilon)$ curve by $(1 - D_{min}) \cos^\zeta\left(\frac{2\varepsilon+U}{2U}\right) + D_{min}$.

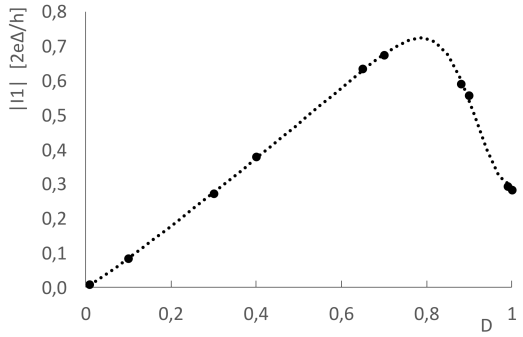

(a) Values of the first Fourier component of the AC Josephson current at $\Delta/2$ read off graphically from Refs. [2] and [15]. The dotted line is an approximation.

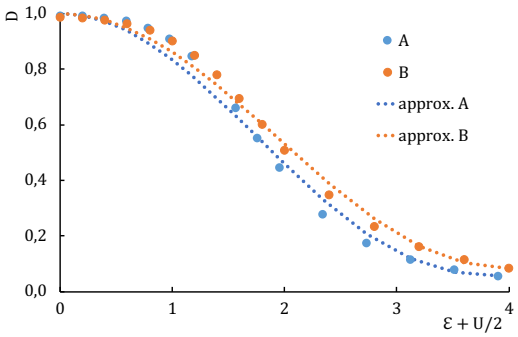

(b) Transmission of the renormalized QPC junction for regions A and B, computed from the ABS energy at $\varphi = \pi$, and approximated by the dotted line.

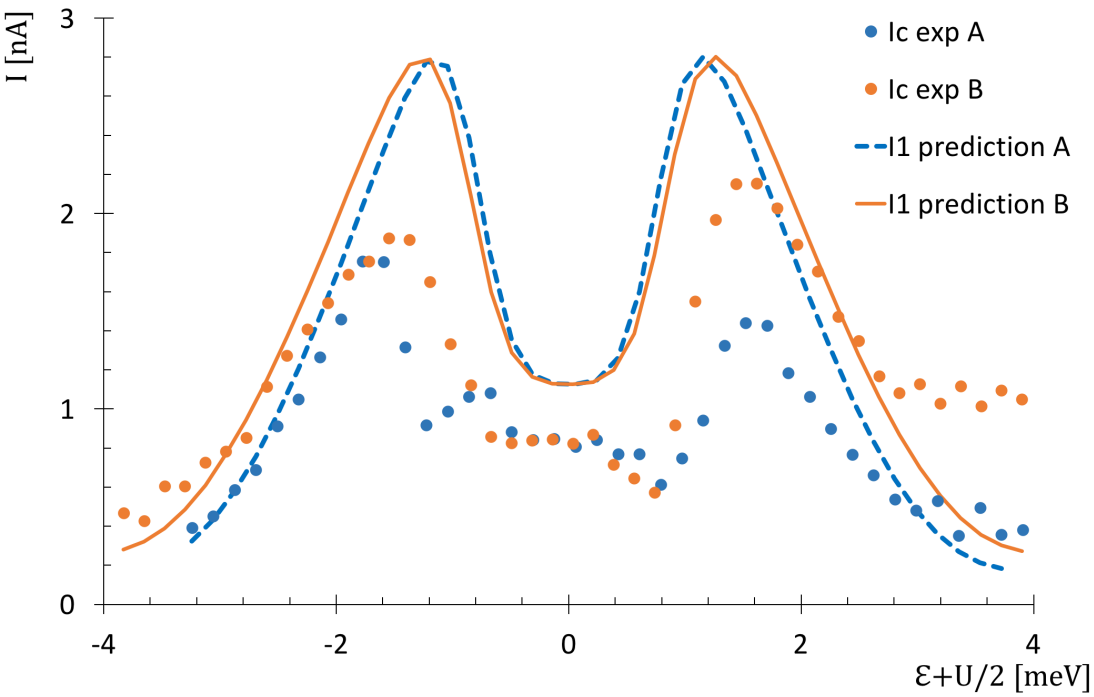

(c) Gate dependence of the first Fourier component $|I_1|$ of the AC Josephson current. Bullets represent the experiment, lines the theoretical prediction for a single quantum point contact with the corresponding transmission.

Figure 2.2.4

Conclusion

This thesis has explored a single-level quantum dot attached to two superconducting leads, described via the superconducting single-impurity Anderson model. I have used analytical techniques and numerical renormalization group calculations.

A major contribution to the large body of previous research is the clarification of the role of coupling asymmetry in the phase-biased (equilibrium) setup. We have been able to link the physics of an asymmetric sc-SIAM system to its effective symmetric counterpart through the symmetry-asymmetry relation. If a physical quantity is known in the symmetric case, it is now possible to derive its value for an asymmetric system analytically. This reduces the need for numerical calculations - it is enough to only compute the symmetric system. Explicit formulas for the phase boundary, on-dot quantities, and the Josephson current are given, and the role of gauge-invariance in deriving the explicit form of the symmetry-asymmetry relation for the Josephson current is specified.

The symmetry-asymmetry relation was applied to find the asymmetry of an experiment from the measured width of the transition region where the current-phase relations are neither fully $0-$ nor fully $\pi-$phase.

This thesis also clarifies to which extent Kondo universality holds for the superconducting quantum dot in a transport setup: The asymmetry turns out to be an important parameter which influences the position of the $0-\pi$ phase boundary even in the Kondo regime. The idea that the phase transition occurs for a fixed Δ/T_K ratio is compromised by its asymmetry and phase dependence. However, the number of parameters can be effectively reduced by one as the superconducting phase difference and the asymmetry are combined into one function by the symmetry-asymmetry relation. We have shown that Kondo universality still holds when using said function as a variable, and the position of the phase boundary deeply in the Kondo regime can be described by a simple exponential formula.

The second topic of this thesis concerns a measurement of the AC Josephson current in a quantum dot setup, specifically the experimentally observed drop in the AC Josephson current in regions where the Kondo effect occurs.

First, the equilibrium many-body spectra and the DC Josephson current are computed to characterize the dot. The dot is found to stay in the $0-$phase and its current-phase relations are almost sinusoidal.

Next, I attempt a quantum-point-contact-based interpretation of the observed drop. A comparison of the many-body spectra of a quantum point contact and the quantum dot is given. Landau-Zener tunneling is considered as a possible cause. The amplitude of the first Fourier component of the AC Josephson current

expected from the exact transport theory of a quantum point contact is also presented. Both methods indicate that a drop in the AC Josephson current is already expected in a QPC, however, taking into account the differences in many-body spectra, we conclude that the mechanisms that cause a drop in the AC Josephson current in a QD are likely different from mechanisms acting in a QPC.

This thesis is a part of the broad research field of superconducting nanostructures. Current endeavors involve the search for exotic matter (Majorana fermions), quantum computing, and the search for a superconducting memory cell. Superconducting quantum dots may serve as basic building blocks for more complicated nanostructures and devices in the near future. It is my hope and belief, that this thesis has contributed to their correct and thorough understanding.

Appendix

Appendix A - Green's functions in Matsubara frequencies

In this appendix, I give some definitions and introduce the Matsubara formalism. The conventions generally correspond to Ref. [6].

The real-time retarded Green's function (for fermionic operators $d_\uparrow$, $d_\downarrow$) is defined as

$$G^R_{d\sigma,d\sigma'}(t'-t) = -i\theta(t-t')\left\langle\left\{d_\sigma(t), d^\dagger_{\sigma'}(t')\right\}\right\rangle \tag{2.2.3}$$

with $\{\}$ marking the anticommutator and $\langle\rangle$ the (grand)canonical average, $\langle\centerdot\rangle = -\frac{1}{Z}\mathrm{Tr}\left[\mathrm{e}^{-\beta\mathrm{H}}\centerdot\right]$, with $H = \mathcal{H} - \mu N$ for grandcanonical averaging. Green's functions are translationally invariant in the time-domain, so that t' can be set to zero. More often, we work in the energy/frequency domain ($\hbar = 1$), using the Fourier transform $G^R_{d\sigma,d\sigma'}(\omega) = \int_{-\infty}^{+\infty} dt\, e^{i\omega t} G^R_{d\sigma,d\sigma'}(t)$. The spectral function is defined as $A_d(\omega) \equiv A_{d\sigma}(\omega) = -2\mathrm{Im}G^R_{d\sigma}(\omega)$. Generally, the density of states corresponds to diagonal elements of a spectral function. In case of the impurity, the spectral function is related to the local density of states (per spin) $\rho_d = \frac{1}{2\pi}A_d(\omega)$ and the occupation number $\overline{n}_d = \int_{-\infty}^{\infty}\frac{d\omega}{2\pi}A_d(\omega)n_F(\omega)$.

For solving equilibrium yet temperature dependent problems, Matsubara frequencies are often advantageous. For this, a transformation into imaginary time

$$t \to -i\tau$$

is done first. This makes it possible to treat temperature in the (grand)canonical averaging and time-dependence of operators similarly, yet induces some counter-intuitive properties like non-hermitian-conjugated operators $d(\tau), d^\dagger(\tau)$ and a necessity to perform an analytic continuation onto the real axis at the end of the calculation. The interaction (Dirac) picture with a Hamiltonian $H = H_0 + V$ is used most often. The time dependence of operators in the imaginary time is governed by $A(\tau) = e^{\tau H_0} A e^{-\tau H_0}$, and the Heisenberg equation reads

$$\frac{\partial A(\tau)}{\partial \tau} = [H,\, A](\tau)\ . \tag{2.2.4}$$

The imaginary-time d-$d^\dagger$ correlation function, or Matsubara Green's function (which, after analytic continuation corresponds to the retarded Green's function) is defined as

$$G_{d\sigma,d\sigma'}(\tau) \equiv -\left\langle T_\tau\left(d_\sigma(\tau)d^\dagger_{\sigma'}\right)\right\rangle \tag{2.2.5}$$

with the time-ordering operator $T_\tau\left[A(\tau)B\right]_\pm = \theta(\tau)A(\tau)B \pm \theta(-\tau)BA(\tau)$ (minus sign for fermionic operators), and $d(\tau) = e^{\tau H_0} d\, e^{-\tau H_0}$. Because of the identity $\mathcal{C}_{dd^\dagger}(\tau+\beta) = -\mathcal{C}_{dd^\dagger}(\tau)$ for $\tau < 0$, only the case $\tau > 0$ needs to be calculated. The thermal averaging $\langle\rangle$ is done using the full Hamiltonian. For quadratic Hamiltonians, the equation of motion technique can be used to find the exact form of the correlation function. For the Matsubara Green's function, eq. (2.2.4) becomes

$$-\partial_\tau G_{d\sigma,d\sigma'}(\tau) = \delta(\tau)\delta_{\sigma,\sigma'} + \left\langle T_\tau\left(\left[H, d_\sigma\right](\tau)\, d^\dagger_{\sigma'}\right)\right\rangle \ . \tag{2.2.6}$$

The Fourier transformation into the Matsubara frequency domain is defined as

$$G_{\mathrm{AB}}(i\omega_n) = \int_0^\beta d\tau e^{i\omega_n\tau} G_{\mathrm{AB}}(\tau) \tag{2.2.7}$$

with the inverse

$$G_{\mathrm{AB}}(\tau) = \frac{1}{\beta}\sum_{\omega_n} e^{-i\omega_n\tau} G_{\mathrm{AB}}(i\omega_n) \tag{2.2.8}$$

with $\omega_n = \frac{2\pi n}{\beta}$ for bosonic operators A, B, and $\omega_n = \frac{(2n+1)\pi}{\beta}$ for fermionic operators.

The (non-interacting, $U = 0$) Green's function of the SIAM

The electron Green's function of a single level interacting with the continuum, $G^{\mathrm{SIAM}}_{0\,d\sigma}(ik_n)$, can be found by the equation of motion technique (the computation starts with Eq. (2.2.6), and can be found in Ref. [6]). In Matsubara frequencies (for one lead and one spin) we obtain

$$G^{\mathrm{SIAM}}_{0\,d\sigma}(ik_n) = \frac{1}{ik_n - \varepsilon_d - \Sigma_0(ik_n)} \tag{2.2.9}$$

with

$$\Sigma_0(ik_n) = \sum_k \frac{|t_k|^2}{ik_n - \varepsilon_k} \tag{2.2.10}$$

The selfenergy can be further simplified using the approximation of a wide, flat band. Assuming $\varepsilon \in [-D,\, D]$ for energies inside the band and $\Gamma \equiv 2\pi \sum_{\mathbf{k}} |t_{\mathbf{k}}|^2 \delta(\varepsilon - \varepsilon_{\mathbf{k}})$ we get

$$\Sigma_0(ik_n) = \frac{\Gamma}{2\pi}\ln\left(\frac{ik_n + D}{ik_n - D}\right) \xrightarrow{D\to\infty} -i\Gamma\,\mathrm{sgn}(k_n)\,, \tag{2.2.11}$$

meaning

$$G^{\mathrm{SIAM}}_{0\,d\sigma}(ik_n) = \frac{1}{ik_n - \varepsilon_d + i\Gamma\,\mathrm{sgn}(k_n)}. \tag{2.2.12}$$

Performing the analytic continuation $ik_n \to \omega + i\eta$ for $k_n > 0$ must reproduce the well-known real-time retarded Green's function for electrons, $G^{R,\,\mathrm{SIAM}}_{0\,d\sigma}(\omega) = 1/\left(\omega - \varepsilon_d + i\Gamma\right)$, cf. eq. (1.1.5) in the main text.

Appendix B - Nambu formalism and the non-interacting Green's function of the superconducting quantum dot

To compute the Green's function of the superconducting quantum dot (see Sec. 1.3.1, Eq. (1.3.1) in the main text for the Hamiltonian), an extended version of the Nambu matrix formalism (often used for superconductivity, see e.g. [6]) is used. Following Appendix A in [49] , infinite Nambu spinors are defined as

$$\alpha(\tau) = \begin{pmatrix} d_{\uparrow}(\tau) \\ d^{\dagger}_{\downarrow}(\tau) \\ c_{L\mathbf{k}\uparrow}(\tau) \\ c^{\dagger}_{L-\mathbf{k}\downarrow}(\tau) \\ c_{Rk\uparrow}(\tau) \\ c^{\dagger}_{R-\mathbf{k}\downarrow}(\tau) \end{pmatrix} \tag{2.2.13}$$

with τ the imaginary time defined in Appendix A. The Nambu Green's function is a generalization of the correlation function in Eq. (2.2.5):

$$\widehat{G}(\tau) = -\left\langle T_{\tau}\alpha(\tau)\,\alpha^{\dagger}(0)\right\rangle . \tag{2.2.14}$$

For the non-interacting dot (see Hamiltonian (1.3.1) with $U = 0$), the Green's function $\widehat{G}_0(i\omega_n)$ can be computed exactly. In that case the equation of motion (2.2.6) takes the form $-\partial_{\tau}\widehat{G}_0(\tau) = \delta(\tau)\mathbb{I} - M\widehat{G}_0(\tau)$ with matrix M

$$M = \begin{pmatrix} -\varepsilon & 0 & -t^{*}_{Lk} & 0 & -t^{*}_{Rk} & 0 \\ 0 & \varepsilon & 0 & t_{Lk} & 0 & t_{Rk} \\ -t_{Lk} & 0 & -\varepsilon_{Lk} & \mathbf{\Delta}_L & 0 & 0 \\ 0 & t^{*}_{Lk} & \mathbf{\Delta}^{*}_L & \varepsilon_{Lk} & 0 & 0 \\ -t_{Rk} & 0 & 0 & 0 & -\varepsilon_{Rk} & \mathbf{\Delta}_R \\ 0 & t^{*}_{Rk} & 0 & 0 & \mathbf{\Delta}^{*}_R & \varepsilon_{Rk} \end{pmatrix} , \tag{2.2.15}$$

where $\mathbf{\Delta}_{L,R} = \Delta_{L,R}e^{i\varphi_{L,R}}$ is the complex order parameter of the left(right) lead, which includes the superconducting phase. This equation is now Fourier-transformed (2.2.7), so that $\partial_{\tau} \to -i\omega_n$, resulting in

$$\widehat{G}_0(i\omega_n) = (i\omega_n + M)^{-1} \tag{2.2.16}$$

It is enough for our purposes to compute the 2x2 upper-left corner of $\widehat{G}_0(i\omega_n)$, representing the quantum dot, or the Fourier-transformed version of

$$\widehat{G}_0(\tau) = \begin{pmatrix} G(\tau) & \mathcal{G}(\tau) \\ \bar{\mathcal{G}}(\tau) & \bar{G}(\tau) \end{pmatrix} = -\begin{pmatrix} \langle T_{\tau}[d_{\uparrow}(\tau)d^{\dagger}_{\uparrow}(0)]\rangle , & \langle T_{\tau}[d_{\uparrow}(\tau)d_{\downarrow}(0)]\rangle \\ \langle T_{\tau}[d^{\dagger}_{\downarrow}(\tau)d^{\dagger}_{\uparrow}(0)]\rangle , & \langle T_{\tau}[d^{\dagger}_{\downarrow}(\tau)d_{\downarrow}(0)]\rangle \end{pmatrix} . \tag{2.2.17}$$

This can be done by applying the matrix partitioning scheme

$$\begin{pmatrix} A & c \\ d & B \end{pmatrix}^{-1} = \begin{pmatrix} (A - cB^{-1}d)^{-1} & -A^{-1}c\,(B - dA^{-1}c)^{-1} \\ -B^{-1}d\,(A - cB^{-1}d)^{-1} & (B - dA^{-1}d)^{-1} \end{pmatrix} \tag{2.2.18}$$

with A corresponding to the 2x2 upper-left corner of $(i\omega_n - M)$ in Eq. (2.2.16), B is an infinite square matrix and c, d are rectangular. Computing the $(A - cB^{-1}d)^{-1}$ combination and integrating out the $k-$dependence assuming $\Gamma_\alpha \equiv \pi \sum_{\mathbf{k}} |t_{\alpha\mathbf{k}}|^2 \delta(\varepsilon - \varepsilon_{\alpha\mathbf{k}})$ constant, we arrive at

$$\widehat{G}_0(i\omega_n) = \begin{pmatrix} i\omega_n[1 + s(i\omega_n)] - \varepsilon \ , & \Delta_\varphi(i\omega_n) \\ \Delta^*_\varphi(i\omega_n) \ , & i\omega_n[1 + s(i\omega_n)] + \varepsilon \end{pmatrix}^{-1} \tag{2.2.19}$$

with $s(i\omega_n) = \sum_\alpha \frac{\Gamma_\alpha}{\sqrt{\Delta_\alpha^2 + \omega_n^2}}$ and $\Delta_\varphi = \sum_\alpha \frac{\Gamma_\alpha}{\sqrt{\Delta_\alpha^2 + \omega_n^2}} \Delta_\alpha e^{i\varphi_\alpha}$, which is Eq. (1.3.6) in the main text.

Appendix C - NRG calculation of sc-SIAM

This appendix contains input files for the NRG calculation. These have been used with the NRG Ljubljana 2.3 and 2.4 versions (in particular 2.4.3.34). An example of the "param" input file:

```
[extra]
Gamma1=0.00214285714
Gamma2=0.00535714286
phi=!(Pi)*0.5

[param]
model=siamphase.m
symtype=SPSU2

bcsgap1=0.0005
bcsgap2=0.0005

U=0.04
delta=0.0
Lambda=4

Tmin=1e-9
keepmin=200
keepenergy=6
keep=10000

discretization=Z
z=1

ops=n_d q_d q_d^2 JC

dumpannotated=100
dumpscaled=0
grouptol=1e-300
```

System parameters U, Γ_L, Γ_R, $\Delta_L = \Delta_R$, φ, and $\delta = \varepsilon + U/2$ are set in this file. All energy scales are set "in units of the bandwidths", meaning $U = 0.04\,D$. For the sc-SIAM, the discretization parameter is set to $\Lambda = 4$. The truncation of the spectra is controlled by either the maximum number of states kept (parameter "keep") or the maximum energy of the states (parameter "keepenergy"), whichever is more restrictive. For the superconducting (gaped) system, it is also important to set a minimum number of states kept in each iteration. The eigenstates are computed and stored, as well as the Josephson current.

The custom model Hamiltonian in Wolfram language using SNEG package, called as siamphase.m in the param file, reads:

```
def2ch[1];

Hc = gammaPolch1 hopphi[f[0], d[], phi/2]
                 + gammaPolch2 hop[f[1], d[]];

H = H0 + H1 + Hc;
```

This defines a two-channel (two leads) model with one impurity site. Hc is the hybridiziation part of the Hamiltionian. The phase difference φ is taken into account by performing a rotation in the Nambu space by $\varphi/2$. This factor then enters the hopping matrix element between channel 1 and the impurity orbital. H0 and H1 describe the (superconducting) lead and the dot and are predefined elsewhere in the code.

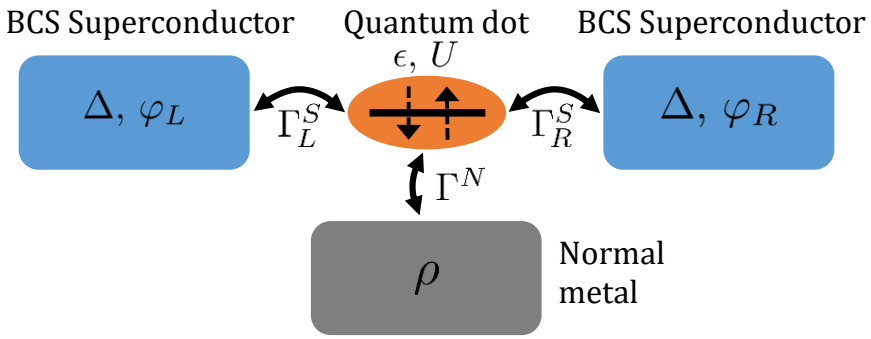

Figure 2.2.5: Schematics of the three-teminal setup.

Appendix D - Lehmann representation for the exchange coupling constant in a three-terminal setup

This Appendix presents a calculation of the exchange coupling constant J in a setup with two superconducting and one normal-metal leads (see Fig. 2.2.5). The coupling to the normal-metal lead is taken as a weak perturbation, while the superconductor-quantum dot-superconductor (S-QD-S) system is described by the sc-SIAM (Hamiltonian (1.3.1)) and mapped onto the Kondo model. The goal is to express J in terms of many-body matrix elements of the operator d and the spectrum which can be calculated by the NRG. The resulting formula hasn't been published or numerically implemented during my studies, but it may be used in future calculations.

The S-QD-S system in the π-phase has a degenerate ground state consisting of many-body states $|\Downarrow\rangle$ and $|\Uparrow\rangle$, denoting eigenstates of the global spin operator. It is also known that the S-QD-S system in certain parameter regimes is governed by Kondo physics. Analogically to the Schrieffer-Wolff transformation in non-superconducting systems, we expect it to be possible to map the S-QD-S system coupled to a normal-metal lead on the Kondo model, and express $J_{k_F k_F}$ in the vicinity of the Fermi level. The Kondo model is described by the Hamiltonian

$$\mathcal{H}_K = \mathcal{H}_N + \mathcal{V}_K = \sum_k \varepsilon_k c_k^\dagger c_k - \sum_{kk'} J_{kk'} \mathbf{S}_d \cdot \mathbf{s}_{kk'} \tag{2.2.20}$$

with the spin operators

$$\mathbf{s}_{kk'} = \sum_{\sigma\sigma'} \frac{1}{2} c_{k\sigma}^\dagger \boldsymbol{\sigma}_{\sigma\sigma'} c_{k'\sigma'} \,, \quad \mathbf{S}_d = \sum_{\sigma\sigma'} \frac{1}{2} d_\sigma^\dagger \boldsymbol{\sigma}_{\sigma\sigma'} d_{\sigma'} \,, \tag{2.2.21}$$

where $c_{k\sigma}^\dagger$, $c_{k\sigma}$ creates/annihilates an electron in the normal-metal probe, $d_\sigma^\dagger$, d_σ on the dot, and $\boldsymbol{\sigma}$ is the vector of Pauli matrices. Using an isotropic Kondo model is based on symmetry considerations – the ground state is (without a magnetic

field) an exactly degenerate spin-doublet, so there is no reason for anisotropy – supported by the result for the atomic limit in Ref. [23].

Our approach is to consider a scattering state and compare the lowest non-zero orders in the T-matrix expansion for the Kondo and the SIAM models. Elements of the T-matrix for a Hamiltonian $\mathcal{H} = \mathcal{H}_0 + \mathcal{V}$ are defined by (see e.g. Ref. [6], page 88)

$$\langle f| T |i\rangle = \langle f| \left(T^{(1)} + T^{(2)} + ...\right) |i\rangle = \langle f| \left(\mathcal{V} + \mathcal{V}\frac{1}{E_i - \mathcal{H}_0 + i\eta}\mathcal{V} + ...\right) |i\rangle \ , \tag{2.2.22}$$

where $|i\rangle$, $|f\rangle$ are the initial and final states, and E_i is the energy of the initial state.

We choose initial and final states

$$\begin{array}{c} |i\rangle = |FS\rangle \, |\Downarrow\rangle \\ |f\rangle = c^\dagger_{k'\downarrow} c_{k\uparrow} \, |FS\rangle \, |\Uparrow\rangle \end{array} \ , \tag{2.2.23}$$

where $|FS\rangle$ denotes the Fermi sea zero-temperature ground state of the normal lead, and $|\Downarrow\rangle$, $|\Uparrow\rangle$ denote the doubly degenerate ground state of the generalized SIAM (in the simplest single-impurity case they're just the up and down states of the impurity spin, but in case of the S-QD-S setup they're complicated many-body states of the dot and the superconducting leads obtained by the NRG).

The impurity part of the Kondo Hamiltonian (2.2.20) in the case of a simple impurity can be expanded to

$$\mathcal{V}_K = -\sum_{ll'} J_{ll'} \frac{1}{2} \left[d^\dagger_\uparrow d_\downarrow c^\dagger_{l\downarrow} c_{l'\uparrow} + d^\dagger_\downarrow d_\uparrow c^\dagger_{l\uparrow} c_{l'\downarrow} + \frac{1}{2} \left(d^\dagger_\uparrow d_\uparrow - d^\dagger_\downarrow d_\downarrow \right) \left(c^\dagger_{l'\uparrow} c_{l\uparrow} - c^\dagger_{l'\downarrow} c_{l\downarrow} \right) \right] .$$

The first order of the T-matrix gives a non-zero result (only the first term of H_K contributes for the choice (2.2.23)), namely

$$\begin{aligned} \langle f| \mathcal{V}_K |i\rangle &= -\sum_{ll'} J_{ll'} \frac{1}{2} \left\{ \langle\uparrow| d^\dagger_\uparrow d_\downarrow |\downarrow\rangle \langle FS| c^\dagger_{k\uparrow} c_{k'\downarrow} c^\dagger_{l\downarrow} c_{l'\uparrow} |FS\rangle \right\} \\ &= -\frac{1}{2} J_{k'k} n_F(k) \left(1 - n_F(k')\right) \end{aligned} \tag{2.2.24}$$

For the generalized SIAM, $\mathcal{H}_0$ is the Hamiltonian of the S-QD-S system (1.3.1) plus the normal lead, and the perturbation $\mathcal{V}$ is the coupling to the normal lead

$$\mathcal{V} = \sum_{p\sigma} \left(V_p c^\dagger_{p\sigma} d_\sigma + V^*_p d^\dagger_\sigma c_{p\sigma} \right) \ .$$

The first order of the T-matrix expansion (2.2.22) for $\mathcal{V}$ is zero, because this perturbation describes no spin flip processes. The first nonzero contribution is

$$\langle f| T^{(2)} |i\rangle = \langle f| \mathcal{V} \frac{1}{E_i - \mathcal{H}_0 + i\eta} \mathcal{V} |i\rangle \ .$$

Using the Lehmann representation, we insert $\mathbb{1} = \sum_{\alpha n} |\alpha n\rangle \langle \alpha n|$, $|\alpha n\rangle = |\alpha\rangle \, |n\rangle$, where $|\alpha\rangle$ are all the eigenstates of the generalized SIAM system and $|n\rangle$ are

normal-metal lead states, and compute

$$\begin{aligned}\langle f|\, T^{(2)}\,|i\rangle &= \sum_{\alpha n}\frac{1}{E_i-E_{\alpha n}+i\eta}\,\langle f|\,\mathcal{V}\,|\alpha n\rangle\,\langle \alpha n|\,\mathcal{V}\,|i\rangle \\ &= \sum_{\alpha n}\frac{1}{E_i-E_{\alpha n}+i\eta}\left\{\sum_{p'\sigma'}V_{p'}\,\langle FS|\,c^\dagger_{k\uparrow}c_{k'\downarrow}c^\dagger_{p'\sigma'}\,|n\rangle\,\langle \Uparrow|\,d_{\sigma'}|\,\alpha\rangle + \right. \\ &\quad \left. + \sum_{p'\sigma'}V^*_{p'}\,\langle FS|\,c^\dagger_{k\uparrow}c_{k'\downarrow}c_{p'\sigma'}\,|n\rangle\left\langle\Uparrow\left|d^\dagger_{\sigma'}\right|\alpha\right\rangle\right\}\times \\ &\quad \times\left\{\sum_{p\sigma}V_p\,\langle n|\,c^\dagger_{p\sigma}\,|FS\rangle\,\langle\alpha\,|d_\sigma|\,\Downarrow\rangle + \sum_{p\sigma}V^*_p\,\langle n|\,c_{p\sigma}\,|FS\rangle\left\langle\alpha\left|d^\dagger_\sigma\right|\Downarrow\right\rangle\right\}\end{aligned}$$

Now it's time to see which states $|n\rangle$ can be reached and also what $E_i - E_{\alpha n}$ is. If the matrix element $\langle n|\,c_{p\sigma}\,|FS\rangle$ is to be non-zero, it forces $|n_1\rangle = c_{p\sigma}\,|FS\rangle$. The initial energy is $E_i = E_N + E_0$, where E_N corresponds to the lead and E_0 to the groundstate $|\Downarrow\rangle$ of the dot. By annihilating an electron, $E_N \to E_N - \varepsilon_p$, so that $E_{\alpha n_1} = E_N - \varepsilon_p + E_\alpha$, and $E_i - E_{\alpha n_1} = E_0 - E_\alpha + \varepsilon_p$. Similarly, for $\langle n|\,c^\dagger_{p\sigma}\,|FS\rangle$ only $|n_2\rangle = c^\dagger_{p\sigma}\,|FS\rangle$ survives, and $E_i - E_{\alpha n_2} = E_0 - E_\alpha - \varepsilon_p$.

From the four terms in the previous expression only two survive (with the right number of c, $c^\dagger$):

$$\begin{aligned}&\langle f|\, T^{(2)}\,|i\rangle = \\ &= \sum_\alpha\sum_{pp'\sigma\sigma'}\left\{\frac{V_{p'}V^*_p}{E_0-E_\alpha+\varepsilon_p+i\eta}\,\langle FS|\,c^\dagger_{k\uparrow}c_{k'\downarrow}c^\dagger_{p'\sigma'}c_{p\sigma}\,|FS\rangle\,\langle\Uparrow|\,d_{\sigma'}|\,\alpha\rangle\left\langle\alpha\left|d^\dagger_\sigma\right|\Downarrow\right\rangle + \right. \\ &\left. + \frac{V^*_{p'}V_p}{E_0-E_\alpha-\varepsilon_p+i\eta}\,\langle FS|\,c^\dagger_{k\uparrow}c_{k'\downarrow}c_{p'\sigma'}c^\dagger_{p\sigma}\,|FS\rangle\left\langle\Uparrow\left|d^\dagger_{\sigma'}\right|\alpha\right\rangle\langle\alpha\,|d_\sigma|\,\Downarrow\rangle\right\}\end{aligned}$$

Working out the contractions, we arrive at

$$\begin{aligned}\langle f|\, T^{(2)}\,|i\rangle = \sum_\alpha&\left\{\frac{\langle\Uparrow|\,d_\downarrow|\,\alpha\rangle\left\langle\alpha\left|d^\dagger_\uparrow\right|\Downarrow\right\rangle}{E_0-E_\alpha+\epsilon_k+i\eta} - \frac{\left\langle\Uparrow\left|d^\dagger_\uparrow\right|\alpha\right\rangle\langle\alpha\,|d_\downarrow|\,\Downarrow\rangle}{E_0-E_\alpha-\epsilon_{k'}+i\eta}\right\} \\ &\times V^*_k V_{k'} n_F(k)(1-n_F(k'))\ .\end{aligned} \tag{2.2.25}$$

Comparing Eq. (2.2.25) to Eq. (2.2.24), the coupling constant $J_{k'k}$ is identified easily

$$J_{k'k} = -2V^*_k V_{k'}\sum_\alpha\left\{\frac{\langle\Uparrow|\,d_\downarrow|\,\alpha\rangle\left\langle\alpha\left|d^\dagger_\uparrow\right|\Downarrow\right\rangle}{E_0-E_\alpha+\epsilon_k+i\eta} - -\frac{\left\langle\Uparrow\left|d^\dagger_\uparrow\right|\alpha\right\rangle\langle\alpha\,|d_\downarrow|\,\Downarrow\rangle}{E_0-E_\alpha-\epsilon_{k'}+i\eta}\right\} \tag{2.2.26}$$

However, there's a problem with formula (2.2.25) to be revealed by comparison to SIAM.

In the simplest case of a bare quantum dot, the states $|\alpha\rangle = \{|0\rangle\,,|\uparrow\rangle\,,|\downarrow\rangle\,,|\uparrow\downarrow\rangle\}$, $E_\alpha = \{0,\,\epsilon_d,\,\epsilon_d,\,2\epsilon_d+U\}$, and $E_0 = \epsilon_d$. The result for the Kondo coupling constant is well known from the Schrieffer-Wolff transformation [59]

$$J^{SW}_{k'k} = V_{k'}V_k\left\{\frac{1}{\varepsilon_d-\varepsilon_k}+\frac{1}{\varepsilon_d-\varepsilon_{k'}}-\frac{1}{\varepsilon_d+U-\varepsilon_k}-\frac{1}{\varepsilon_d+U-\varepsilon_{k'}}\right\}\ . \tag{2.2.27}$$

Formula (2.2.26) is evaluated as follows:

$$\begin{aligned} \langle\uparrow |d_\downarrow| \alpha_1\rangle \left\langle \alpha_1 \left| d_\uparrow^\dagger \right| \downarrow \right\rangle &= -1 \qquad & E_{\alpha 1} &= 2\epsilon_d + U \\ \left\langle \uparrow \left| d_\uparrow^\dagger \right| \alpha_2 \right\rangle \langle \alpha_2 |d_\downarrow| \downarrow\rangle &= 1 & E_{\alpha 2} &= 0 \end{aligned}$$

leading to

$$J_{k'k} = -2V_k^* V_{k'} \left\{ \frac{1}{\varepsilon_d + U - \varepsilon_k} - \frac{1}{\varepsilon_d - \varepsilon_{k'}} \right\} ,$$

which is not exactly Eq. (2.2.27). To obtain $J_{k'k}^{SW}$, one has to symmetrize (2.2.26) in k, k'. After symmetrization, the formula gives the correct $J_{kk'}$ also for the three-terminal setup in the $\Delta \longrightarrow \infty$ as calculated in [23].

The relevant scattering happens at the Fermi level, and after setting $\varepsilon_k = \varepsilon_{k'} = \varepsilon_{k_F} = 0$, we obtain

$$\frac{J_{k_F k_F} \rho_N}{\Gamma_N} = \frac{J_{k_F k_F}}{\pi |V_{k_F}|^2} = \frac{1}{\pi} \sum_\alpha \frac{\left\langle \Uparrow \left| d_\uparrow^\dagger \right| \alpha \right\rangle \langle \alpha |d_\downarrow| \Downarrow\rangle - \langle \Uparrow |d_\downarrow| \alpha\rangle \left\langle \alpha \left| d_\uparrow^\dagger \right| \Downarrow \right\rangle}{E_0 - E_\alpha} \tag{2.2.28}$$

The small positive imaginary part has been omitted in the denominator.

List of Abbreviations

ABS	Andreev bound state(s)
BCS	Bardeen-Cooper-Schrieffer
CPR	Current-phase relations
DOS	Density of states
LZ	Landau-Zener
NRG	Numerical renormalization group
sc-	Superconducting
SIAM	Single-impurity Anderson model
S-QD-S	Superconductor-Quantum dot-Superconductor
QD	Quantum dot
QMC	Quantum Monte Carlo
QPC	Quantum point contact

List of Publications

Paper I A. Kadlecová, M. Žonda, and T. Novotný. *Quantum dot attached to superconducting leads: Relation between symmetric and asymmetric coupling.* Physical Review B **95**, 195114 (2017).

Paper II A. Kadlecová, M. Žonda, V. Pokorný, and T. Novotný. *Practical guide to quantum phase transitions in quantum-dot-based tunable Josephson junctions.* Physical Review Applied **11**, 044094 (2019).

Paper III D. Watfa, R. Delagrange, A. Kadlecová, M. Ferrier, A. Kasumov, H. Bouchiat, and R. Deblock. *Collapse of the Josephson emission in a carbon nanotube junction in the Kondo regime.* Physical Review Letters **126**, 126801 (2021).

All published articles are attached to this thesis.

Also see Appendix D for an unpublished calculation of the exchange coupling constant J in a three-terminal setup.

Bibliography

[1] Anderson, P. W. Localized magnetic states in metals. *Phys. Rev. 124*, 1 (1961), 41–53.

[2] Averin, D., and Bardas, A. ac Josephson effect in a single quantum channel. *Physical Review Letters 75*, 9 (1995), 1831–1834.

[3] Basset, J., Bouchiat, H., and Deblock, R. Emission and absorption quantum noise measurement with an on-chip resonant circuit. *Physical Review Letters 105*, 16 (2010), 166801.

[4] Basset, J., Delagrange, R., Weil, R., Kasumov, A., Bouchiat, H., and Deblock, R. Joint measurement of current-phase relations and transport properties of hybrid junctions using a three junctions superconducting quantum interference device. *Journal of Applied Physics 116*, 024311 (2014).

[5] Beenakker, C. W. J., and van Houten, H. Josephson current through a superconducting quantum point contact shorter than the coherence length. *Physical Review Letters 66*, 23 (1991), 3056–3059.

[6] Bruus, H., and Flensberg, K. *Many-Body Quantum Theory in Condensed Matter Physics: An Introduction.* Oxford Graduate Texts. Oxford University Press, 2004.

[7] Buitelaar, M. R., Nussbaumer, T., and Schönenberger, C. Quantum dot in the Kondo regime coupled to superconductors. *Phys. Rev. Lett. 89*, 25 (2002), 256801.

[8] Buizert, C., Oiwa, A., Shibata, K., Hirakawa, K., and Tarucha, S. Kondo universal scaling for a quantum dot coupled to superconducting leads. *Phys. Rev. Lett. 99* (2007), 136806.

[9] Bulla, R., Costi, T. A., and Pruschke, T. Numerical renormalization group method for quantum impurity systems. *Rev. Mod. Phys. 80*, 2 (2008), 395–450.

[10] Chang, W., Manucharyan, V. E., Jespersen, T. S., Nygård, J., and Marcus, C. M. Tunneling spectroscopy of quasiparticle bound states in a spinful Josephson junction. *Phys. Rev. Lett. 110*, 21 (2013), 217005.

[11] Charlier, J.-C., Blase, X., and Roche, S. Electronic and transport properties of nanotubes. *Reviews of Modern Physics 79*, 2 (2007), 677–732.

[12] Choi, M.-S., Lee, M., Kang, K., and Belzig, W. Kondo effect and Josephson current through a quantum dot between two superconductors. *Phys. Rev. B 70*, 2 (2004), 020502.

[13] Choi, M.-S., Lee, M., Kang, K., and Belzig, W. Comment on "Josephson current through a nanoscale magnetic quantum dot". *Phys. Rev. Lett. 94*, 22 (2005), 229701.

[14] Cleuziou, J. P., Wernsdorfer, W., Bouchiat, V., Ondarcuhu, T., and Monthioux, M. Carbon nanotube superconducting quantum interference device. *Nat. Nanotechnol. 1*, 1 (2006), 53–59.

[15] Cuevas, J. C., Martín-Rodero, A., and Yeyati, A. L. Hamiltonian approach to the transport properties of superconducting quantum point contacts. *Physical Review B 54*, 10 (1996), 7366–7379.

[16] Cuevas, J. C., and Scheer, E. *Molecular Electronics: An Introduction to Theory and Experiment*, vol. 1 of *World Scientific Series in Nanoscience and Nanotechnology*. WORLD SCIENTIFIC, 2010.

[17] De Franceschi, S., Kouwenhoven, L., Schönenberger, C., and Wernsdorfer, W. Hybrid superconductor-quantum dot devices. *Nat. Nanotechnol. 5*, 10 (2010), 703–711.

[18] de Gennes, P. G. *Superconductivity of metals and alloys*. W.A. Benjamin, Inc., 1966.

[19] Delagrange, R. *Josephson effect and high frequency emission in a carbon nanotube in the Kondo regime*. PhD thesis, Universite Paris-Sud, 2016.

[20] Delagrange, R., Luitz, D. J., Weil, R., Kasumov, A., Meden, V., Bouchiat, H., and Deblock, R. Manipulating the magnetic state of a carbon nanotube Josephson junction using the superconducting phase. *Phys. Rev. B 91* (2015), 241401(R).

[21] Delagrange, R., Weil, R., Kasumov, A., Ferrier, M., Bouchiat, H., and Deblock, R. 0-π quantum transition in a carbon nanotube Josephson junction: Universal phase dependence and orbital degeneracy. *Phys. Rev. B 93*, 19 (2016), 195437.

[22] Dell'Anna, L., Zazunov, A., and Egger, R. Superconducting nonequilibrium transport through a weakly interacting quantum dot. *Physical Review B 77*, 10 (2008), 104525.

[23] Domański, T., Žonda, M., Pokorný, V., Górski, G., Janiš, V., and Novotný, T. Josephson-phase-controlled interplay between correlation effects and electron pairing in a three-terminal nanostructure. *Physical Review B 95*, 4 (2017), 045104.

[24] Eichler, A., Deblock, R., Weiss, M., Karrasch, C., Meden, V., Schönenberger, C., and Bouchiat, H. Tuning the Josephson current in carbon nanotubes with the Kondo effect. *Phys. Rev. B 79*, 16 (2009), 161407.

[25] Glazman, L. I., and Matveev, K. A. Resonant Josephson current through Kondo impurities in a tunnel barrier. *JETP Lett. 49*, 10 (1989), 659.

[26] Governale, M., Pala, M. G., and König, J. Real-time diagrammatic approach to transport through interacting quantum dots with normal and superconducting leads. *Phys. Rev. B 77*, 13 (2008), 134513.

[27] Greiter, M. Is electromagnetic gauge invariance spontaneously violated in superconductors? *Annals of Physics 319*, 1 (2005), 217–249.

[28] Haldane, F. D. M. Theory of the atomic limit of the Anderson model. I. perturbation expansions re-examined. *J. Phys. C 11*, 24 (1978), 5015.

[29] Hiltscher, B., Governale, M., and König, J. ac Josephson transport through interacting quantum dots. *Physical Review B 86*, 23 (2012), 235427.

[30] Houzet, M., Meyer, J. S., Badiane, D. M., and Glazman, L. I. Dynamics of Majorana states in a topological Josephson junction. *Physical Review Letters 111*, 4 (2013), 046401.

[31] Jørgensen, H. I., Novotný, T., Grove-Rasmussen, K., Flensberg, K., and Lindelof, P. E. Critical current $0 - \pi$ transition in designed Josephson quantum dot junctions. *Nano Lett. 7*, 8 (2007), 2441–2445.

[32] Karrasch, C., Oguri, A., and Meden, V. Josephson current through a single Anderson impurity coupled to BCS leads. *Phys. Rev. B 77*, 2 (2008), 024517.

[33] Kasumov, A. Y., Deblock, R., Kociak, M., Reulet, B., Bouchiat, H., Khodos, I. I., Gorbatov, Y. B., Volkov, V. T., Journet, C., and Burghard, M. Supercurrents through single-walled carbon nanotubes. *Science 284*, 5419 (1999), 1508–1511.

[34] Kouwenhoven, L., and Glazman, L. I. Revival of the Kondo effect. *Physics World 14*, 1 (2001), 33–38.

[35] Laird, E. A., Kuemmeth, F., Steele, G. A., Grove-Rasmussen, K., Nygård, J., Flensberg, K., and Kouwenhoven, L. P. Quantum transport in carbon nanotubes. *Reviews of Modern Physics 87*, 3 (2015), 703–764.

[36] Lamic, B., Meyer, J. S., and Houzet, M. Josephson radiation in a superconductor-quantum dot-superconductor junction. *Physical Review Research 2*, 3 (2020), 033158.

[37] Likharev, K. K. *Dynamics of Josephson Junctions and Cirquits*. No. ISBN 3-88124-042-9. Gordon and Breach Publishers, 1986.

[38] Lindemann, S., Ihn, T., Heinzel, T., Zwerger, W., Ensslin, K., Maranowski, K., and Gossard, A. C. Stability of spin states in quantum dots. *Phys. Rev. B 66* (2002), 195314.

[39] Luitz, D. J., and Assaad, F. F. Weak-coupling continuous-time quantum Monte Carlo study of the single impurity and periodic Anderson models with s-wave superconducting baths. *Phys. Rev. B 81*, 2 (2010), 024509.

[40] Luitz, D. J., Assaad, F. F., Novotný, T., Karrasch, C., and Meden, V. Understanding the Josephson current through a Kondo-correlated quantum dot. *Phys. Rev. Lett. 108*, 22 (2012), 227001.

[41] Mahan, G. D. *Many-particle physics*. Plenum, New York, 2000.

[42] Martín-Rodero, A., and Levy Yeyati, A. Josephson and Andreev transport through quantum dots. *Adv. Phys. 60*, 6 (2011), 899–958.

[43] Maurand, R., Meng, T., Bonet, E., Florens, S., Marty, L., and Wernsdorfer, W. First order $0 - \pi$ quantum phase transition in the Kondo regime of a superconducting carbon nanotube quantum dot. *Phys. Rev. X 2*, 1 (2012), 011009.

[44] Meden, V. The Anderson–Josephson quantum dot—a theory perspective. *Journal of Physics: Condensed Matter 31*, 16 (2019), 163001.

[45] Meng, T. Andreev bound states in Josephson quantum dot devices. Master's thesis, Institut Néel, CNRS Grenoble, 2009.

[46] Meng, T., Florens, S., and Simon, P. Self-consistent description of Andreev bound states in Josephson quantum dot devices. *Phys. Rev. B 79*, 22 (2009), 224521.

[47] Metzner, W., Salmhofer, M., Honerkamp, C., Meden, V., and Schönhammer, K. Functional renormalization group approach to correlated fermion systems. *Reviews of Modern Physics 84*, 1 (2012), 299–352.

[48] Morpurgo, A. F., Kong, J., Marcus, C. M., and Dai, H. Gate-controlled superconducting proximity effect in carbon nanotubes. *Science 286*, 5438 (1999), 263–265.

[49] Novotný, T., Rossini, A., and Flensberg, K. Josephson current through a molecular transistor in a dissipative environment. *Phys. Rev. B 72*, 22 (2005), 224502.

[50] Oguri, A., Tanaka, Y., and Bauer, J. Interplay between Kondo and Andreev-Josephson effects in a quantum dot coupled to one normal and two superconducting leads. *Phys. Rev. B 87* (2013), 075432.

[51] Pallecchi, E., Gaass, M., Ryndyk, D. A., and Strunk, C. Carbon nanotube Josephson junctions with Nb contacts. *Appl. Phys. Lett. 93*, 7 (2008), 072501–3.

[52] Pershoguba, S. S., Veness, T., and Glazman, L. I. Landauer formula for a superconducting quantum point contact. *Physical Review Letters 123*, 6 (2019), 067001.

[53] Pillet, J.-D., Joyez, P., Žitko, R., and Goffman, M. F. Tunneling spectroscopy of a single quantum dot coupled to a superconductor: From Kondo ridge to Andreev bound states. *Phys. Rev. B 88*, 4 (2013), 045101.

[54] Pillet, J.-D., Quay, C. H. L., Morfin, P., Bena, C., Yeyati, A. L., and Joyez, P. Andreev bound states in supercurrent-carrying carbon nanotubes revealed. *Nat. Phys. 6*, 12 (2010), 965–969.

[55] Pokorný, V., and Žonda, M. Correlation effects in superconducting quantum dot systems. *Physica B 536* (2018), 488–491.

[56] Sakai, O., Shimizu, Y., Shiba, H., and Satori, K. Numerical renormalization group study of magnetic impurities in superconductors. II. dynamical excitation spectra and spatial variation of the order parameter. *Journal of the Physical Society of Japan 62*, 9 (1993), 3181–3197.

[57] Satori, K., Shiba, H., Sakai, O., and Shimizu, Y. Numerical renormalization group study of magnetic impurities in superconductors. *Journal of the Physical Society of Japan 61*, 9 (1992), 3239–3254.

[58] Schindele, J., Baumgartner, A., Maurand, R., Weiss, M., and Schönenberger, C. Nonlocal spectroscopy of Andreev bound states. *Phys. Rev. B 89* (2014), 045422.

[59] Schrieffer, J. R., and Wolff, P. A. Relation between the Anderson and Kondo hamiltonians. *Phys. Rev. 149* (1966), 491–492.

[60] Shiba, H. A Hartree-Fock theory of transition-metal impurities in a superconductor. *Prog. Theor. Phys. 50*, 1 (1973), 50–73.

[61] Siano, F., and Egger, R. Josephson current through a nanoscale magnetic quantum dot. *Phys. Rev. Lett. 93*, 4 (2004), 047002.

[62] Siano, F., and Egger, R. Erratum: Josephson current through a nanoscale magnetic quantum dot [phys. rev. lett. 93, 047002 (2004)]. *Phys. Rev. Lett. 94*, 3 (2005), 039902.

[63] Siano, F., and Egger, R. Siano and egger reply:. *Phys. Rev. Lett. 94*, 22 (2005), 229702.

[64] Svensson, S. F. *Thermoelectric phenomena in quantum dots*. PhD thesis, Lund University, 2014.

[65] Tinkham, M. *Introduction to superconductivity.* McGraw–Hill, New York, 1996.

[66] van Dam, J. A., Nazarov, Y. V., Bakkers, E. P. A. M., De Franceschi, S., and Kouwenhoven, L. P. Supercurrent reversal in quantum dots. *Nature 442*, 7103 (2006), 667–670.

[67] Vecino, E., Buitelaar, M. R., Martín-Rodero, A., Schönenberger, C., and Levy Yeyati, A. Conductance properties of nanotubes coupled to superconducting leads: Signatures of Andreev states dynamics. *Solid State Communications 131*, 9 (2004), 625–630.

[68] Vecino, E., Martín-Rodero, A., and Yeyati, A. L. Josephson current through a correlated quantum level: Andreev states and π junction behavior. *Phys. Rev. B 68*, 3 (2003), 035105.

[69] Watfa, D. *Supercurrent and dynamics in carbon nanotube Josephson Junction in the Kondo regime.* PhD thesis, Université Paris-Saclay, 2020.

[70] Wilson, K. G. The renormalization group: Critical phenomena and the Kondo problem. *Rev. Mod. Phys. 47* (1975), 773–840.

[71] Yeyati, A. L., Martín-Rodero, A., and Vecino, E. Nonequilibrium dynamics of Andreev states in the Kondo regime. *Physical Review Letters 91*, 26 (2003), 266802–.

[72] Yoshioka, T., and Ohashi, Y. Numerical renormalization group studies on single impurity Anderson model in superconductivity: A unified treatment of magnetic, nonmagnetic impurities, and resonance scattering. *J. Phys. Soc. Jpn. 69*, 6 (2000), 1812–1823.

[73] Zhang, Y., Liu, G., and Lau, C. Phase diffusion in single-walled carbon nanotube Josephson transistors. *Nano Res. 1*, 2 (2008-08-01), 145–151.

[74] Žitko, R. NRG Ljubljana - open source numerical renormalization group code, available from nrgljubljana.ijs.si. nrgljubljana.ijs.si.

[75] Žitko, R. *Many-particle effects in resonant tunneling of electrons through nanostructures.* PhD thesis, University of Ljubljana, 2007.

[76] Žitko, R. SNEG – Mathematica package for symbolic calculations with second-quantization-operator expressions. *Computer Physics Communications 182*, 10 (2011), 2259–2264.

[77] Žitko, R., and Pruschke, T. Energy resolution and discretization artifacts in the numerical renormalization group. *Phys. Rev. B 79* (2009), 085106.

[78] Žonda, M., Pokorný, V., Janiš, V., and Novotný, T. Perturbation theory of a superconducting $0 - \pi$ impurity quantum phase transition. *Sci. Rep. 5* (2015), 8821.

[79] Žonda, M., Pokorný, V., Janiš, V., and Novotný, T. Perturbation theory for an Anderson quantum dot asymmetrically attached to two superconducting leads. *Phys. Rev. B 93* (2016), 024523.